

AD_____

Award Number: W81XWH-04-1-0554

TITLE: SAPHIRE: A New Flat-Panel Digital Mammography Detector with Avalanche Photoconductor and High-Resolution Field Emitter Readout

PRINCIPAL INVESTIGATOR: Wei Zhao, Ph.D.

CONTRACTING ORGANIZATION: The Research Foundation
State University of New York
Albany, NY 12201-0009

REPORT DATE: June 2006

TYPE OF REPORT: Annual

PREPARED FOR: U.S. Army Medical Research and Materiel Command
Fort Detrick, Maryland 21702-5012

DISTRIBUTION STATEMENT: Approved for Public Release;
Distribution Unlimited

The views, opinions and/or findings contained in this report are those of the author(s) and should not be construed as an official Department of the Army position, policy or decision unless so designated by other documentation.

REPORT DOCUMENTATION PAGE

*Form Approved
OMB No. 0704-0188*

Public reporting burden for this collection of information is estimated to average 1 hour per response, including the time for reviewing instructions, searching existing data sources, gathering and maintaining the data needed, and completing and reviewing this collection of information. Send comments regarding this burden estimate or any other aspect of this collection of information, including suggestions for reducing this burden to Department of Defense, Washington Headquarters Services, Directorate for Information Operations and Reports (0704-0188), 1215 Jefferson Davis Highway, Suite 1204, Arlington, VA 22202-4302. Respondents should be aware that notwithstanding any other provision of law, no person shall be subject to any penalty for failing to comply with a collection of information if it does not display a currently valid OMB control number. PLEASE DO NOT RETURN YOUR FORM TO THE ABOVE ADDRESS.

1. REPORT DATE 01-06-2006			2. REPORT TYPE Annual			3. DATES COVERED 15 May 2005 – 14 May 2006		
4. TITLE AND SUBTITLE SAPHIRE: A New Flat-Panel Digital Mammography Detector with Avalanche Photoconductor and High-Resolution Field Emitter Readout			5a. CONTRACT NUMBER					
			5b. GRANT NUMBER W81xwh-04-1-0554					
			5c. PROGRAM ELEMENT NUMBER					
6. AUTHOR(S) Wei Zhao, Ph.D.			5d. PROJECT NUMBER					
			5e. TASK NUMBER					
			5f. WORK UNIT NUMBER					
7. PERFORMING ORGANIZATION NAME(S) AND ADDRESS(ES) The Research Foundation State University of New York Albany, NY 12201-0009			8. PERFORMING ORGANIZATION REPORT NUMBER					
9. SPONSORING / MONITORING AGENCY NAME(S) AND ADDRESS(ES) U.S. Army Medical Research and Materiel Command Fort Detrick, Maryland 21702-5012			10. SPONSOR/MONITOR'S ACRONYM(S)					
			11. SPONSOR/MONITOR'S REPORT NUMBER(S)					
12. DISTRIBUTION / AVAILABILITY STATEMENT Approved for Public Release; Distribution Unlimited								
13. SUPPLEMENTARY NOTES Original contains colored plates: ALL DTIC reproductions will be in black and white.								
14. ABSTRACT A new concept of flat-panel imager (FPI) with avalanche gain and high resolution (with 50 micron pixel size) is being investigated for improving the imaging performance of digital mammography at low dose and high spatial frequencies, which are critical for the detection of subtle breast abnormalities and the development of digital tomosynthesis. The detector employs an avalanche photoconductor – amorphous selenium (a-Se), called HARP, to detect and amplify the optical signal generated by a structured scintillator - cesium iodide (CsI), and form a charge image that is read out by a high-resolution field emitter array (FEA). We call the proposed detector SAPHIRE (Scintillator-Avalanche Photoconductor with High Resolution Emitter readout). Our investigation showed that the avalanche gain of SAPHIRE permits the use of high resolution (HR) type CsI, which has not been used in existing FPI due to its low light output. HR CsI can provide better imaging performance at high spatial frequencies than existing digital mammography detectors. We also investigated the factors affecting the resolution and image lag of the FEA readout method. Our results showed that adding electrostatic focusing at the FEA substrate can significantly improve the image resolution and lag of the detector. Dividing the signal electrode into multiple (e.g. 32) strips will improve both the electronic noise and the readout speed of the detector.								
15. SUBJECT TERMS Breast Cancer								
16. SECURITY CLASSIFICATION OF:			UU	18. NUMBER OF PAGES 33	19a. NAME OF RESPONSIBLE PERSON USAMRMC			
a. REPORT U	b. ABSTRACT U	c. THIS PAGE U			19b. TELEPHONE NUMBER (include area code)			

Table of Contents

Cover.....	1
SF 298.....	2
Introduction.....	4
Body.....	4
Key Research Accomplishments.....	8
Reportable Outcomes.....	8
Conclusions.....	9
References.....	9
Appendices.....	10

INTRODUCTION:

A new concept of flat-panel imager (FPI) with avalanche gain and high resolution (with 50 micron pixel size) is being investigated for improving the imaging performance of digital mammography at low dose and high spatial frequencies, which are critical for the detection of subtle breast abnormalities and the development of digital tomosynthesis. The detector employs an avalanche photoconductor – amorphous selenium (a-Se), which is called HARP, to detect and amplify the optical signal generated by an x-ray scintillator with needle structure - cesium iodide (CsI), and form a charge image that is read out by a high-resolution field emitter array (FEA). We call the proposed detector SAPHIRE (Scintillator-Avalanche Photoconductor with High Resolution Emitter readout). Our objective is to investigate the feasibility of SAPHIRE and demonstrate its potential advantages over existing detector technology.

BODY:

The following tasks were proposed in the approved Statement of Work. The results of our investigation in the first year are summarized as follows:

TASK 1: Determine the optimal CsI-HARP combination for mammography, Month 1-24

- a. Develop a linear system model for SAPHIRE, so that the imaging performance of different CsI-HARP combination can be predicted. Month 1-6

In order to determine the optimal CsI layer for SAPHIRE, we investigated the imaging performance of four different samples of CsI layers with thickness of 150 μm , which is appropriate for mammography. The CsI samples differ in their manufacturing methods. Two were optimized for high resolution (HR) and the other two were optimized for high light (HL). For each type (HR or HL) of CsI, two different substrates were used. The samples with fiber optic face plate were called FOS, and the samples with amorphous carbon substrates were called ACS. We found that ACS HR plate has higher light output than the FOS HR plate, however it has slightly lower Swank factor (i.e. higher added noise) due to the higher variance in light output for x-rays absorbed at different depth of the CsI layer. This is directly related to the method of manufacturing of the CsI samples. This investigation has generated a lot of interests from the manufacturer, Hamamatsu Photonics, and we will be collaborating on the optimization of CsI manufacturing methods for different x-ray imaging applications. This work is described in detail in a Med. Phys. paper published earlier this year (manuscript 1).

- b. Make a test system for experimental measurement of the imaging performance of CsI-HARP combination using a HARP tube with fiber optic faceplate. Month 1-12

We made an improved HARP tube with FOP faceplate. It has much fewer defects than the first one made last year, the thickness of the HARP layer was increased to 7 μm (from the 4 μm last year). Shown in Figure 1 (left) is a picture of the FOP HARP tube installed in an NTSC standard camera with separate high voltage control for the target.

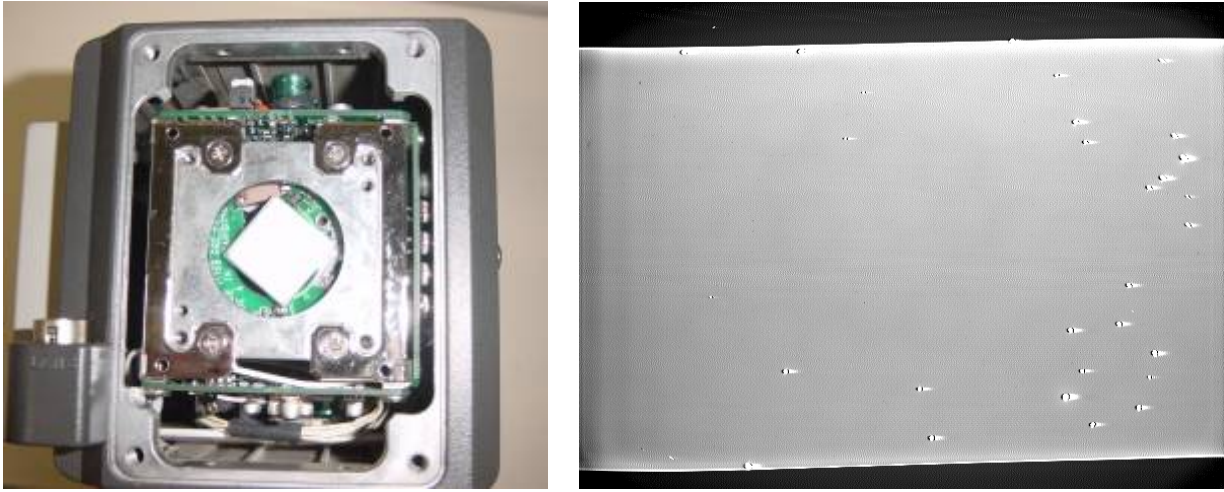


Figure 1: Left: Improved prototype FOP HARP tube installed in a NTSC camera. The FOP face plate is in direct contact with a CsI layer at the front surface. Right: a flat field x-ray image made with the CsI-FOP HARP combination, point defects are visible.

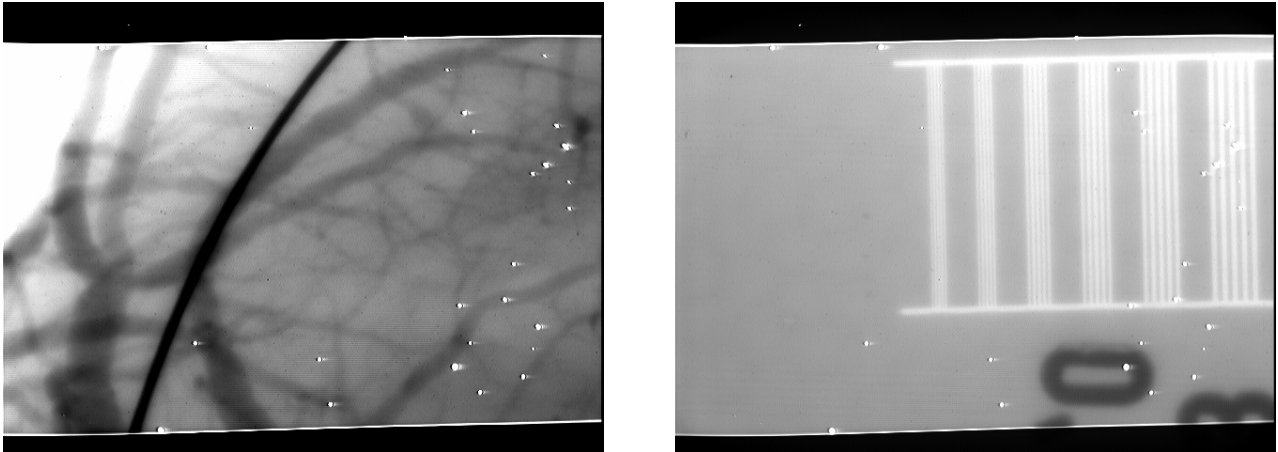


Figure 2: X-ray images obtained with the prototype FOP HARP directly coupled to a CsI layer (150 μm HL type). Left: image of a dog heart and a 180 μm thick wire; Right: x-ray image of a bar pattern. The resolution of the bars from right to left are: 6.3, 8, 10, 12.5, 16 and 20 lp/mm, respectively. It shows that the bars with 16 lp/mm are visible.

- c. Measure the x-ray imaging performance of CsI-HARP using CsI of different types and thickness, and determine the optimal CsI-HARP combination. Month 13-24

A 150 μm thick CsI layer (HL type optimized for maximum light output) was coupled directly to the FOP faceplate for x-ray detection. Shown in Figure 1 (right) is a flat-field x-ray image made with the CsI coupled FOP HARP. The gain of the HARP tube is approximately 60. Only several point defects are visible on the right hand side of the active imaging area, which is a significant improvement over the large area of defects of the previous prototype. This was made possible by mechanical polishing of the FOP prior to soft (optical) polishing before HARP deposition. This prototype FOP HARP tube would allow us to conduct systematic characterization of the imaging properties of the CsI-HARP

combination. Figure 2 (left) shows an x-ray image of a dog heart with a 180 μm wire, and Figure 2 (right) is the image of a resolution bar pattern. It shows that while the FOP coupling between CsI and HARP is able to preserve the resolution, there is some image blur mostly caused by the inherent image resolution of the CsI layer, which is optimized for light output. These preliminary results are encouraging. We are going to start a full characterization of the MTF, NPS and DQE of different CsI layers in combination with HARP, and determine the advantage of avalanche gain, as predicted in our theoretical investigation.

TASK 2: Investigate the factors affecting the spatial resolution of the FEA readout method, Month 1-36

- a. Develop an electric field simulation for the electron optics of SAPHIRE to calculate the electron beam trajectory for FEA readout method. Month 1-12
- b. Determine the optimal mesh electrode configuration that results in the highest spatial resolution. Month 13-18
- c. Refine optimal mesh electrode configuration in connection with the noise model. Month 19-21
- d. Calculate the spatial resolution due to FEA readout for the prototype detector to verify experimental measurement. Month 25-36

Our previous studies showed that by placing the HARP target and the FEA close to each other (0.5 mm) and applying a high mesh voltage that is >400 V, the lateral spreading of the electron beam emitted from the FEA could be limited to < 50 μm . However it is very challenging in practice to maintain a vacuum spacing of 0.5 over a large area, practical distance is usually \sim 1 mm. Furthermore, the electron beam spread is a function of signal charge, which makes the images non-uniform.

Therefore we conducted further investigation of the methods for improving spatial resolution of SAPHIRE. Our simulation showed that by adding an integrated focusing electrode on the FEA, the electron beam spread can be limited to within 2 μm , which makes the size of the electron beam defined by the pixel size of the FEA instead of the lateral spread. Shown in Figure 3 are the results of our simulation, which is the trajectory of electrons emitted from the FEA ($y=0$) before reaching the HARP target. ($y=1000 \mu\text{m}$). The distance between HARP and FEA was 1 mm, with a mesh voltage of 350 V. It shows that without focusing electrode, the lateral spread of the electron beam emitted from each FEA tip is \sim 60 μm (per side), which is not appropriate for pixel sizes < 100 μm . With the focusing electrode, which is an integrated electrode held at negative potential above the gate electrode of the FEA, the lateral spread of the electron beam is significantly reduced.

A manuscript is currently being prepared for submission entitled: “SAPHIRE (Scintillator-Avalanche Photoconductor with High Resolution Emitter readout) for X-ray Imaging: Spatial Resolution and Lag”. It includes our theoretical investigation of the factors affecting the spatial resolution and image lag of SAPHIRE.

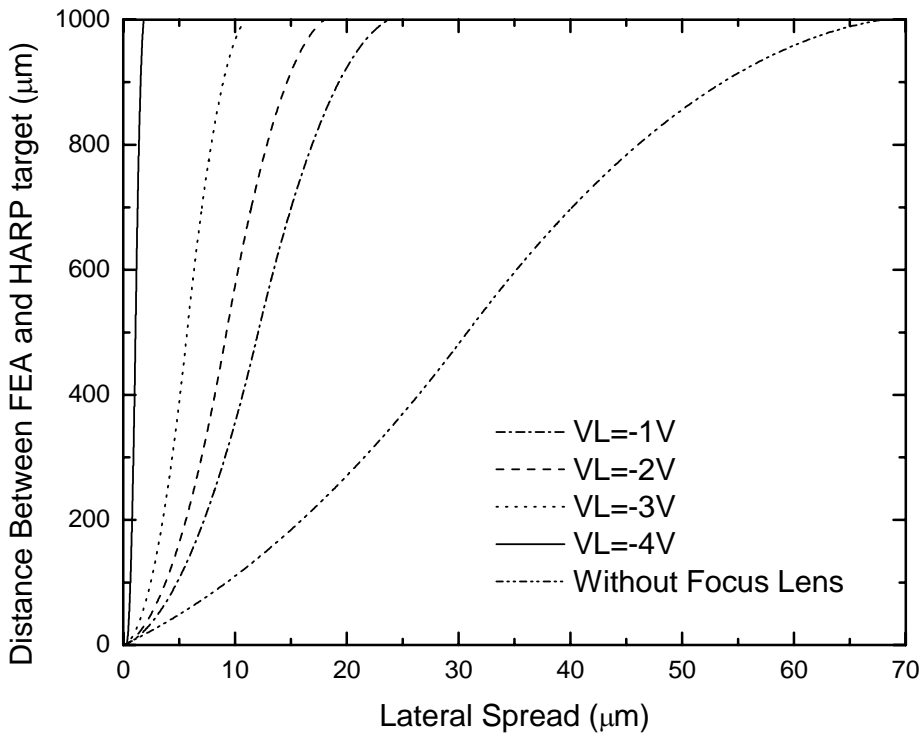


Figure 3: Simulated electron trajectory for FEA-HARP distance of 1 mm. The mesh is placed in the center, i.e. 0.5 mm from the FEA and HARP, and held at 350 V (not shown in the graph). The lateral spread of electrons exceeds 60 μm on each side. With the focusing electrode held at a negative potential VL , the beam spread depends can be reduced to $< 2\mu\text{m}$.

TASK 3: Investigate the factors affecting the electronic noise and readout speed, Month 1-21

- a. Investigate the factors affecting the readout speed of SAPHIRE and determine the readout time as a function of the number of ITO stripes and characteristics of charge amplifier ASIC. Month 7-12
- b. Investigate the factors affecting the electronic noise and develop a noise model based on the properties of charge amplifiers, the number of divided ITO stripes, the readout speed and the electron optics design. Month 13-18
- c. Optimize the number of stripes and the mesh electrode configuration so that the best noise performance and adequate readout speed can be achieved. Month 19-21

We determined that in order to keep the electronic noise below 2000 electrons, the ITO signal electrode for HARP should be divided into strips. For a full field digital mammography detector of 24 cm x 30 cm, dividing into 32 strips is sufficient to keep the amplifier input load capacitance $< 50 \text{ pF}$, which leads to an amplifier noise of < 2000 electrons. Division of the signal electrode also permits parallel readout of signal by firing 32 FEA pixels at the same time. Although readout speed in mammography is not demanding at 30 second per image, the new development of digital

tomosynthesis requires a frame rate of 3 frames / second. The readout lag of SAPHIRE will be dominated by the beam discharge lag of the electrons, which is a function of the energy spread of the electron beam and the thickness of HARP. Figure 4 shows the first frame beam discharge lag as a function of frame time for two different target thickness values. We assumed that the ITO electrode of HARP is divided into 32 strips, and the pixel size is 50 μm . This means that the detector has 6000 x 4800 pixels, and each strip serves as the signal electrode for 6000 x 150 pixels. Figure 4 shows that for a HARP thickness of 8 μm and a frame rate of 3 frames per second, the first frame lag (at 300 ms) is less than 2 %. For a thicker target with smaller capacitance, the lag is negligible.

TASK 4: Demonstrate the practical feasibility of SAPHIRE by building a small area prototype detector, Month 22-36

- a. Construct the small area prototype detector according to the optimal mesh electrode configuration determined from TASK 3. Month 22-24
- b. Evaluate the optical imaging performance of the prototype detector without CsI at the input. Month 25-27
- c. Evaluate the x-ray imaging performance of the prototype detector with CsI coupled to the input. Month 28-36

KEY RESEARCH ACCOMPLISHMENTS:

- Developed a cascaded linear system model for SAPHIRE.
- Investigated the imaging performance of CsI layers made with different manufacturing techniques, and determined that the CsI optimized for high resolution (HR) can provide better DQE at higher spatial frequencies required for mammography. It was also discovered that HR CsI deposited on FOP substrates provides the highest Swank factor, whereas HR CsI on amorphous carbon substrate provides higher light output at the cost of a lower Swank factor.
- Investigated the factors affecting the spatial resolution and image lag. Determined that dividing the ITO signal electrode of a full field digital mammography detector into 32 strips is sufficient for a readout speed of 3 frames per second, and keeping the electronic noise to < 2000 electrons.
- Constructed a prototype HARP tube with FOP substrate, which can be coupled directly to different types of CsI layers.

REPORTABLE OUTCOME:

Manuscripts:

1. Wei Zhao, Dan Li, Alla Reznik, B. J. M. Lui, D. C. Hunt, J. A. Rowlands, Yuji Ohkawa and Kenkichi Tanioka, “Indirect flat-panel detector with avalanche gain: Fundamental feasibility investigation for SHARP-AMFPI (Scintillator HARP Active Matrix Flat Panel Imager)”, Med. Phys. 2954-2966 (2005)

2. A. R. Lubinsky, Wei Zhao, Goran Ristic and J. A. Rowlands, "Screen optics effects on detective quantum efficiency in digital radiography: Zero-frequency effects", Med. Phys. **33**, 1499-1509 (2006)
3. A. Reznik, B. J. M. Lui, Y. Ohkawa, T. Matsubara, K. Miyakawa, M. Kubota, K. Tanioka, T. Kawai, W. Zhao and J. A. Rowlands, "The quantum effience of photo-charge generation in a-Se avalanche photodetectors", Nuclear Instrument and Methods A (accepted)

Conference presentations and published abstract:

- 1 Dan Li, Wei Zhao, Geordi Pang and J. A. Rowlands, "A new concept of indirect flat-panel detector: SAPHIRE (Scintillator Avalanche Photoconductor with High Resolution Emitter readout)", AAPM Annual Conference, August, 2005, Seattle, WA

CONCLUSIONS

During the second year of our research supported by Army BCRP, we have focused our investigation on understanding the factors affecting the spatial resolution, image lag and electronic noise of SAPHIRE. We found that adding a focusing electrode at each FEA tip can reduce the lateral spreading of the electron beam from 60 μm to 2 μm . The focusing electrode allows the distance between HARP and the FEA to be kept at a practical distance, i.e. 1 mm or more, and the potential of the mesh electrode reasonably low, e.g. 350 V, while maintaining a high resolution that is defined by the pixel size of the FEA array. By dividing the ITO signal electrode to a moderate number of strips, e.g. 32, the electronic noise can be kept below 2000 electrons, and the readout rate of a full field digital mammography detector with 50 μm pixel size could be 3 frames per second or higher.

REFERENCES

Indirect flat-panel detector with avalanche gain: Fundamental feasibility investigation for SHARP-AMFPI (scintillator HARP active matrix flat panel imager)

Wei Zhao^{a)} and Dan Li

Department of Radiology, State University of New York at Stony Brook, L-4, 120 Health Sciences Center
Stony Brook, New York 11793-8460

Alla Reznik, B. J. M. Lui, D. C. Hunt, and J. A. Rowlands

Imaging Research, Sunnybrook and Women's Health Sciences Center, 2075 Bayview Avenue, Toronto,
Ontario, M4N 3M5 Canada

Yuji Ohkawa and Kenkichi Tanioka

Advanced Imaging Devices Research Division, Science & Technical Research Laboratories,
Japan Broadcasting Corporation, 1-10-11 Kinuta, Setagaya-ku, Tokyo 157-8510 Japan

(Received 11 April 2005; revised 30 June 2005; accepted for publication 30 June 2005;
published 30 August 2005)

An indirect flat-panel imager (FPI) with avalanche gain is being investigated for low-dose x-ray imaging. It is made by optically coupling a structured x-ray scintillator CsI(Tl) to an amorphous selenium (*a*-Se) avalanche photoconductor called HARP (high-gain avalanche rushing photoconductor). The final electronic image is read out using an active matrix array of thin film transistors (TFT). We call the proposed detector SHARP-AMFPI (scintillator HARP active matrix flat panel imager). The advantage of the SHARP-AMFPI is its programmable gain, which can be turned on during low dose fluoroscopy to overcome electronic noise, and turned off during high dose radiography to avoid pixel saturation. The purpose of this paper is to investigate the important design considerations for SHARP-AMFPI such as avalanche gain, which depends on both the thickness d_{Se} and the applied electric field E_{Se} of the HARP layer. To determine the optimal design parameter and operational conditions for HARP, we measured the E_{Se} dependence of both avalanche gain and optical quantum efficiency of an 8 μm HARP layer. The results were used in a physical model of HARP as well as a linear cascaded model of the FPI to determine the following x-ray imaging properties in both the avalanche and nonavalanche modes as a function of E_{Se} : (1) total gain (which is the product of avalanche gain and optical quantum efficiency); (2) linearity; (3) dynamic range; (4) gain nonuniformity resulting from thickness nonuniformity; and (5) effects of direct x-ray interaction in HARP. Our results showed that a HARP layer thickness of 8 μm can provide adequate avalanche gain and sufficient dynamic range for x-ray imaging applications to permit quantum limited operation over the range of exposures needed for radiography and fluoroscopy. © 2005 American Association of Physicists in Medicine.

[DOI: 10.1118/1.2008428]

Key words: flat-panel detectors, avalanche gain, amorphous selenium, cesium iodide

I. INTRODUCTION

An active matrix flat-panel imager (AMFPI) based on thin film transistor (TFT) arrays is the most promising technology for digital x-ray imaging due to its compact size, rapid readout, and superior performance compared to screen films.¹ AMFPI are categorized as either *direct* or *indirect* based on the materials used for x-ray detection (x-ray photoconductors or scintillators, respectively). Direct AMFPI has the advantages of higher image resolution and a simpler TFT array structure that can be manufactured in a standard facility for active matrix liquid crystal displays (AMLCD). Despite their differences, both types of AMFPI offer better image quality than screen films and computed radiography (CR).^{2,3}

However before AMFPI can equal the performance of the x-ray image intensifier (XRII) in fluoroscopy, two major difficulties must be overcome: (i) the ability to produce good

image quality at a very low dose, such as in the dark part of a fluoroscopy image ($\sim 0.1 \mu\text{R}$ per frame)^{4,5} and (ii) the ability to produce images at a high frame rate without artifacts, especially when the radiation exposure is switched from radiographic to fluoroscopic.^{6,7} Even in well-established radiographic applications, AMFPI are facing challenges because their rapid readout and freedom from geometric distortion have generated a renewed interest in advanced clinical applications. One example is digital tomosynthesis,⁸ in which a rapid sequence of images is taken from different angles, and tomographic slices at different depths of the patient anatomy are reconstructed. The application of AMFPI in cone-beam computed tomography^{9,10} (CT) is also under intensive investigation. Such advanced applications of AMFPI pose challenges for the development of the next generation of detectors, primarily regarding the ability of AMFPI to generate

high quality images that are quantum noise limited and free from artifacts at low x-ray exposures and high frame rates. It has been shown that the detective quantum efficiency (DQE) of AMFPI is inferior to XR II at the lower end of the dose range ($0.1\text{--}1 \mu\text{R}$ per frame) encountered in fluoroscopy.¹¹ In mammography, the detector is not x-ray quantum noise limited behind dense breast, where the average exposure is $\sim 1 \text{ mR}$, and the DQE of the detector is severely compromised by the electronic noise.^{12,13}

The strategies for improving the low dose performance of AMFPI can be divided into two categories: one is to increase the x-ray to image charge conversion gain so that the x-ray quantum noise can overcome the electronic noise and the other is to decrease the electronic noise. These strategies are common to both types of AMFPI since they have approximately the same conversion gain and pixel electronic noise.¹ Several investigations are taking place to increase the gain for direct AMFPI by developing other x-ray photoconductors. Promising results have been shown for lead iodide (PbI_2) and mercuric iodide (HgI_2).¹⁴ The conversion gain of these two materials is 5–7 times higher than that of current systems. The challenges for this technology are to develop deposition techniques for large area detectors with good imaging properties, and to ensure that both electrons and holes have adequate range to reduce the probability of charge trapping.¹⁵ To reduce electronic noise, several investigators have proposed advanced pixel designs, which incorporate pixel amplification by adding at least two more TFTs at each pixel.^{16–18} The electronic noise can thus be reduced to ~ 700 electrons per pixel, which is a factor of 2–4 lower than existing AMFPI. A challenge for this approach is the practical implementation of the complex pixel design over a large area with consistent and uniform imaging performance because each pixel operates as an analog amplifier circuit as opposed to the simple switching device (digital) in existing AMFPI. Due to these practical challenges none of the above approaches for increased gain and reduced electronic noise has been implemented in commercial large area AMFPI.

We are proposing a new concept of AMFPI by adding avalanche gain to an indirect AMFPI, as shown in Fig. 1. The optical photons emitted from the CsI layer upon absorption of x rays are detected and amplified by an avalanche $a\text{-Se}$ photoconductor called HARP (high-gain avalanche rushing photoconductor). Light photons absorbed by the HARP layer generate electron-hole pairs near the top interface ($<0.1 \mu\text{m}$). Under a sufficiently high E_{Se} (produced by applying positive voltage on the top bias electrode of $a\text{-Se}$), holes moving toward the bottom surface will undergo avalanche multiplication and create more holes and electrons. The avalanche gain g_{av} ranges from unity up to ~ 1000 times depending on E_{Se} and the thickness of the $a\text{-Se}$ layer, d_{Se} .¹⁹ The electrons move to the top bias electrode while holes are collected by the pixel electrodes and form a charge image, which is readout with a two-dimensional array of TFTs, similar to that in existing AMFPI. The proposed detector is named SHARP-AMFPI (scintillator-HARP active matrix flat-panel imager). Rougeot and Possin have suggested a

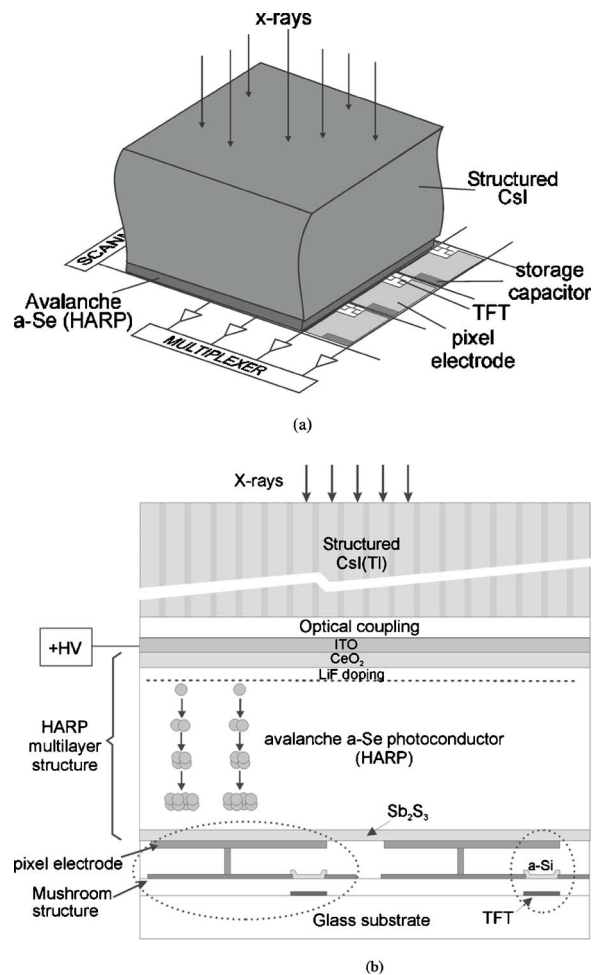


FIG. 1. (a) Diagram showing the concept of SHARP-AMFPI, where an avalanche photoconductor is used to detect light photons generated by CsI. (b) Side view showing the multilayer structure of the detector (thickness not drawn to scale).

similar concept,²⁰ but it has not been implemented. The only other indirect AMFPI approach involving an $a\text{-Se}$ photoconductor as an optical sensor did not have avalanche gain.²¹

Compared to existing indirect FPI, SHARP-AMFPI has the following advantages: (1) x-ray quantum noise limited at a much lower x-ray exposure level; (2) better temporal performance, i.e., lower lag and ghosting because of the lower trap density in $a\text{-Se}$ (compared to $a\text{-Si}$) and the much higher electric field E_{Se} ; (3) compatibility with standard TFT array manufacturing facility for AMLCD; (4) ability to use high-resolution (HR) type CsI, which cannot be used in existing AMFPI due to its lower light output. Compared to the high conversion gain x-ray photoconductors being developed for direct FPI, the proposed detector has the following advantages: (1) *Programmable* gain by changing the electric field E_{Se} as opposed to the fixed high conversion gain of HgI_2 or PbI_2 . One of the practical problems of having a fixed high gain is that the large signal charge (at high exposure) requires a large pixel storage capacitor ($>15 \text{ pF}$), which is impractical to make especially for small pixel sizes. This means that a detector that is optimized for low dose (fluoroscopic) x-ray imaging applications will not work properly at

high radiographic dose levels. With SHARP-AMFPI, by appropriately decreasing the E_{Se} during high exposure applications, the signal charge is comparable to that at low dose with avalanche gain. This simplifies the TFT array pixel design and permits a detector with wide dynamic range. (2) Better temporal performance because both charge carriers in $a\text{-Se}$ have adequate range and the probability of charge trapping is low. This is in contrast to the very short range of one type of carriers in PbI_2 (electrons) and HgI_2 (holes) which results in significant charge trapping and ghosting. The advantages described above make the proposed detector suitable for all x-ray imaging modalities (i.e., radiography and fluoroscopy). The purpose of this paper is to investigate the important design parameters for HARP and to establish the operational conditions that ensure adequate dynamic range for both fluoroscopy and radiography.

Since avalanche multiplication in $a\text{-Se}$ was discovered over a decade ago the HARP video tube, which consists of a HARP layer readout with a scanning electron beam, has been commercialized for high sensitivity and high definition television applications. Stable and uniform avalanche multiplication has been demonstrated with very little added noise.²² No correction for fixed pattern noise is necessary. The electric field E_{Se} under which avalanche multiplication occurs is $>70 \text{ V}/\mu\text{m}$, which is an order of magnitude higher than that typically used in direct AMFPI incorporating thick $a\text{-Se}$ layers. To sustain E_{Se} of this high magnitude without a significant increase in dark current due to charge injection from the bias electrodes, blocking layers are required for both electrode interfaces. As shown in Fig. 1(b), the HARP sensor is a multilayer structure.¹⁹ It contains a transparent indium tin oxide (ITO) electrode which is biased positively during imaging, followed by a thin layer ($\sim 20 \text{ nm}$) of cerium oxide (CeO_2) and a thin layer of lithium fluoride (LiF) doped $a\text{-Se}$ to block injection of holes from the ITO. The intrinsic $a\text{-Se}$ photoconductor is from 0.5 to $35 \mu\text{m}$ thick depending on the desired avalanche gain. The bottom interface of the HARP structure is a submicron thin layer of antimony trisulfide (Sb_2S_3), which is used to block electron injection from the negative bias electrode (i.e., pixel electrodes of the TFT array). Since the mobility of holes in $a\text{-Se}$ is more than 30 times higher than that of electrons, only holes create a significant number of carriers by impact ionization. Hence it is essential for light photons to enter from the positive bias electrode.

Our previous calculation using a preliminary linear system model of indirect FPI with avalanche gain predicted that an avalanche gain of $g_{av}=20$ is needed to produce x-ray quantum noise limited performance for fluoroscopy and low dose mammography (tomosynthesis).²³ The avalanche gain of HARP increases as a function of both the electric field E_{Se} and the thickness d_{Se} . To minimize dark current E_{Se} is usually $\leq 120 \text{ V}/\mu\text{m}$. A value of $g_{av}=20$ requires a HARP layer thickness of $4 \mu\text{m}$ or above.²⁴ For the present paper we investigated the effects of the optical imaging properties of HARP on the x-ray imaging performance of SHARP-AMFPI, so that appropriate design parameters and opera-

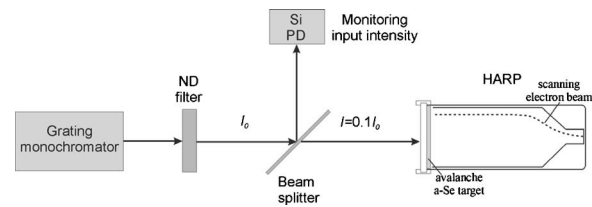


FIG. 2. Experimental apparatus for measuring the photosensitivity of HARP.

tional conditions could be determined. We measured the E_{Se} dependence of both avalanche gain and optical quantum efficiency of an $8 \mu\text{m}$ HARP layer. The results were used in a physical model of HARP as well as a linear cascaded model of the FPI to determine the following x-ray imaging properties in both the avalanche and nonavalanche modes as a function of d_{Se} and E_{Se} : (1) total gain (which is the product of avalanche gain and optical quantum efficiency); (2) linearity; (3) dynamic range; (4) gain nonuniformity resulting from thickness nonuniformity; and (5) the effects of direct x-ray interaction in HARP.

II. PHOTOSENSITIVITY OF HARP

The x-ray imaging performance of indirect FPI with avalanche gain relies on the photosensitivity of HARP. Understanding the dependence of photosensitivity on E_{Se} and the layer thickness d_{Se} is crucial for guiding the choice of HARP design parameters and operational conditions for both the avalanche and nonavalanche modes. In this section, we will first present the experimental method and results of the HARP photosensitivity measurements, and then describe the theory of E_{Se} dependence of photosensitivity, which is proportional to both the optical quantum efficiency (QE) η and the avalanche gain g_{av} . The theory and experimental data will then be used to determine η and g_{av} as a function of E_{Se} in the context of x-ray imaging.

A. Experimental measurement of photosensitivity

1. Method

The experimental apparatus for photosensitivity measurement is shown in Fig. 2. A grating monochromator was used to generate optical photons of a single wavelength λ . The values of λ used in our experiments were in the range of 380–600 nm. The intensity of the output beam was attenuated by neutral-density (ND) filters. A beamsplitter was used to direct a fraction (90%) of the attenuated beam to a silicon (Si) photodiode (PD), which was used to monitor the beam intensity during the experiment. The optical photons passing directly through the beam splitter (10%) were detected by the HARP video tube. Before photosensitivity measurements the input light intensity to the HARP was calibrated such that a constant input power was used for each λ . This was achieved by adjustment of the ND filters based on the light intensity monitored by the Si PD.

For each λ and E_{Se} , the signal current S from the HARP tube was recorded. The photosensitivity was quantified as the number of signal charge carriers generated per absorbed light

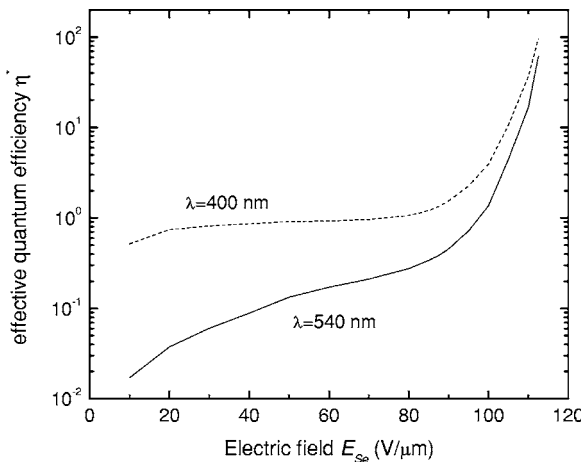


FIG. 3. Measured effective quantum efficiency η^* as a function of E_{Se} for an 8 μm thick HARP layer.

photon. This is referred to as the effective quantum efficiency η^* , and it is the product of η and g_{av} . The values of η^* were experimentally determined from the measurement of HARP tube current S using

$$\eta^* = \frac{S/e}{IT_s/h\nu} \quad (1)$$

where e is the electron charge, I is the HARP input light intensity power given in Watts (W), $h\nu$ is the energy of each incident photon, and T_s is the fraction of the photons incident on the HARP tube reaching the a -Se layer. The correction factor T_s represents the light attenuation by the glass faceplate, the ITO bias electrode and the CeO_2 blocking layer for HARP. The value of T_s is a function of the wavelength λ and was experimentally measured using a HARP substrate consisting just of the faceplate, electrode, and blocking layer. During the manufacture of HARP targets this structure is assembled prior to deposition of the a -Se layer. The substrate sample was placed in the beam path of the monochromator and the transmission of light was calculated by taking the ratio of the light intensity measured by the Si PD with the sample in place and that without.

2. Measurement results

The measured effective quantum efficiency η^* is shown in Fig. 3 as a function of E_{Se} for an 8 μm thick HARP layer. For blue light ($\lambda=400$ nm), η^* reaches a plateau at $E_{Se} > 20$ V/ μm . This corresponds to a saturation of optical quantum efficiency η at unity. With a further increase in E_{Se} to >80 V/ μm , η^* starts to increase again, which shows the onset of avalanche. However for green light, the E_{Se} dependence of η^* is quite different. As shown in Fig. 3 for $\lambda = 540$ nm, which is the peak of the emission spectrum of CsI (Tl), η^* starts at a much smaller value compared to that for blue light. It then increases continuously with E_{Se} without reaching a plateau before avalanche begins at ~ 80 V/ μm . This is because the optical η for green light is lower and does not reach unity until E_{Se} is well into the range of ava-

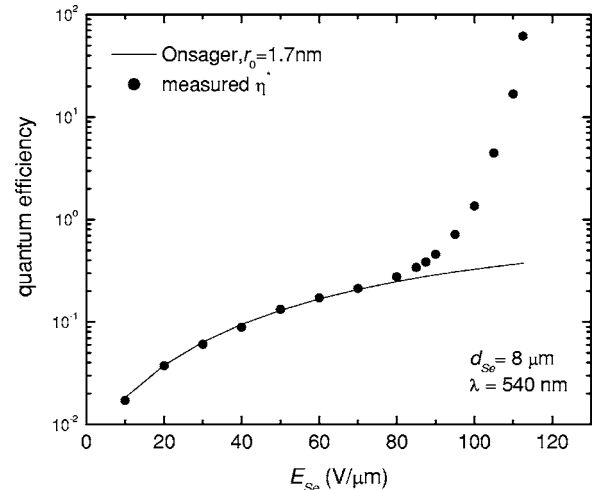


FIG. 4. Optical quantum efficiency of a -Se calculated using Onsager theory and $r_0=1.7$ nm, compared with the measured effective quantum efficiency η^* at $\lambda=540$ nm.

lanche multiplication. To choose the proper operational condition for HARP in different x-ray imaging applications, we need to understand separately the E_{Se} dependence of η and g_{av} . This will be discussed in Sec. II B.

B. Determination of quantum efficiency and avalanche gain

The effective quantum efficiency η^* of HARP is proportional to both η and g_{av} . The value of η in a -Se depends on both E_{Se} and the wavelength λ of the incident photon. It was found by Pai and Enck that the E_{Se} and λ dependence of photogeneration in a -Se follow the Onsager mechanism.²⁵ Onsager theory states that every absorbed photon creates a pair of thermalized carriers bound by their Coulombic attraction. The initial separation r_0 of the charge pair increases with incident photon energy. The probability of dissociation for the bound pairs into free carriers increases with r_0 and the applied external field E_{Se} with the relationship

$$\eta = \phi_0 \frac{kT}{eE_{Se}r_0} e^{-A} e^{-eE_{Se}r_0/kT} \sum_{m=0}^{\infty} \frac{A^m}{m!} \sum_{n=0}^{\infty} \sum_{l=m+n+1}^{\infty} \left(\frac{eE_{Se}r_0}{kT} \right)^l \frac{1}{l!},$$

$$\text{with } A = \frac{e^2}{4\pi\epsilon\epsilon_0 kT}, \quad (2)$$

where ϕ_0 is defined as the efficiency of production of thermalized charge pairs per absorbed photon and is independent of E_{Se} . Pai and Enck showed that the room temperature measurement of η can be best fitted with the expression in Eq. (2) using $\phi_0=1$ and r_0 in the range between 0.8 and 7.0 nm for λ values between 620 and 400 nm. For the rest of the discussion in this paper, we will focus on $\lambda=540$ nm, which is the peak of the emission spectrum for CsI (Tl). Shown in Fig. 4 are the values of η calculated using Eq. (2) and $r_0 = 1.7$ nm. Also plotted in Fig. 4 are the η^* measured at the same wavelength for $d_{Se}=8$ μm . These results show that the Onsager theory provides a reasonable prediction for the E_{Se}

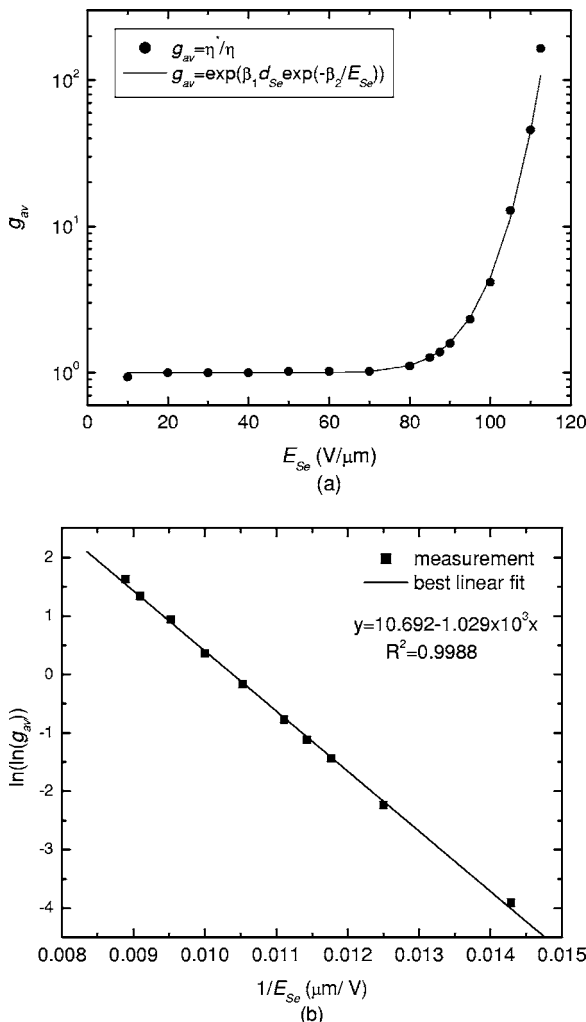


FIG. 5. (a) Solid circles are the g_{av} for the 8 μm HARP layer calculated by dividing the measured η^* at 540 nm by the optical η predicted by the Onsager theory using $r_0=1.7$ nm. The solid line shows the g_{av} calculated using the fitted β_1 and β_2 values. (b) The plot of $\ln(\ln g_{av})$ as a function of $1/E_{Se}$, and the best linear fit for the data.

dependence of η^* in HARP for $E_{Se} \leq 70$ where $g_{av}=1$. The calculated η using Onsager theory was then divided into the measured η^* so that the E_{Se} dependence of avalanche gain g_{av} can be obtained. The results are shown in Fig. 5(a), where $g_{av}=46$ at $E_{Se}=110$ V/ μm . Figure 5(a) shows that g_{av} increases very rapidly with E_{Se} hence choosing the appropriate E_{Se} for HARP is crucial. To determine the x-ray response of SHARP-AMFPI it is necessary to understand the continuous dependence of g_{av} on E_{Se} because as image charge accumulates on the pixels, the voltage drop across the HARP layer will decrease. This change in E_{Se} will produce a corresponding change in g_{av} and affect the x-ray sensitivity, linearity, and dynamic range of the FPI.

The avalanche gain characteristics in HARP have been investigated as a function of d_{Se} and E_{Se} .²⁶ According to the theory of avalanche multiplication,²⁷ when E_{Se} across the thickness d_{Se} is uniform, and the distance through which avalanche occurs is equal to d_{Se} (which is true for an 8 μm

HARP because photons are absorbed within 0.1 μm at the entrance side of the a -Se layer), g_{av} is given by²⁸

$$g_{av} = \frac{(\beta - \alpha)e^{d_{Se}(\beta - \alpha)}}{\beta - \alpha e^{d_{Se}(\beta - \alpha)}}, \quad (3)$$

where α and β are the impact ionization coefficients of electrons and holes, respectively. In a -Se the value of β is much greater than α since the drift mobility of holes (0.18 cm 2 /Vs) is much higher than that of electrons (0.003 cm 2 /Vs). This is why in HARP light always enters from the positive bias electrode to maximize avalanche gain. It is important to note that in order for g_{av} [as defined in Eq. (3)] to have a finite positive value, i.e., stable avalanche, the condition of $\beta > \alpha e^{(\beta - \alpha)d_{Se}}$ must be satisfied. Under the assumption that the contribution of electrons to avalanche gain is negligible, Eq. (3) can be simplified to

$$g_{av} = e^{d_{Se}\beta} \quad (4)$$

with β given by

$$\beta = \beta_1 e^{-\beta_2/E_{Se}}. \quad (5)$$

The values for β_1 and β_2 can be determined by curve fitting of experimental measurement of g_{av} . By taking the logarithms of both sides of Eq. (4) twice, we obtain

$$\ln(\ln g_{av}) = \ln(\beta_1 d_{Se}) - \frac{\beta_2}{E_{Se}}, \quad (6)$$

which indicates that the quantity $\ln(\ln g_{av})$ is linearly related to $1/E_{Se}$. Shown in Fig. 5(b) is the experimentally determined g_{av} data from Fig. 5(a) replotted in the form of $\ln(\ln g_{av})$ as a function of $1/E_{Se}$. The best linear fit to the experimental data is also shown in Fig. 5(b). From the intercept and the slope of the fitted line we obtained $\beta_1=5.5 \times 10^3 \mu\text{m}^{-1}$ and $\beta_2=1.029 \times 10^3 \text{ V}/\mu\text{m}$. Using these β_1 and β_2 values and the analytical expression for g_{av} shown in Eqs. (4) and (5), the fitted g_{av} values were calculated and are shown in Fig. 5(a). It shows that the calculated g_{av} using the fitted parameters agrees well with experimentally determined g_{av} for $E_{Se} \leq 110$ V/ μm . Hence the fitted parameters β_1 and β_2 will be used in the following investigation of the potential x-ray imaging performance of SHARP-AMFPI.

III. POTENTIAL X-RAY IMAGING PERFORMANCE

A. Cascaded linear system model for SHARP-AMFPI

Previously we have developed a cascaded linear system model for indirect FPI with avalanche gain.²³ This preliminary investigation did not include K-fluorescence reabsorption in CsI or direct x-ray interaction in HARP. We showed that the DQE(f) is related to the avalanche gain g_{av} through

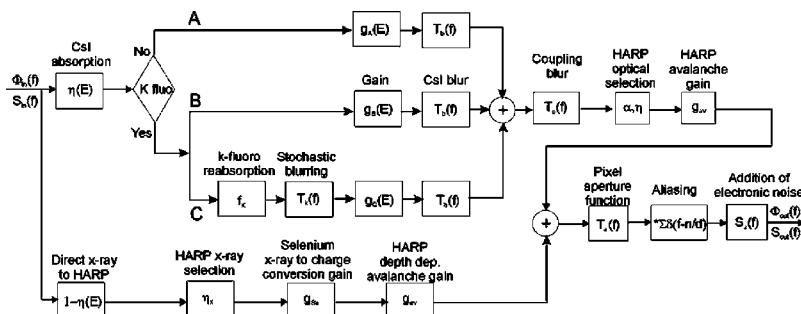


FIG. 6. Flow diagram showing the serial and parallel stages of the cascaded linear system model for SHARP-AMFPI.

$$DQE(f) = \frac{T_b^2(f) T_c^2(f) T_a^2(f)}{\left[\frac{1}{\eta_x A_S} T_b^2(f) T_c^2(f) + \frac{(2g_{av}-1)}{g_{av} g \eta_x \gamma \eta} \right] T_a^2(f) + \frac{S_n}{(a_p^2 g_{av} g \eta_x \gamma \eta)^2 q_0}}, \quad (7)$$

where q_0 is the number of incident x-ray photons per unit area, γ is the optical coupling efficiency between CsI and the HARP layer, $T_b(f)$, $T_c(f)$, and $T_a(f)$ are the MTFs due to blur in CsI, the optical coupling between CsI and HARP, and the pixel aperture function, respectively. A_S , η_x , and g are the Swank factor, x-ray quantum absorption efficiency, and x-ray to photon conversion gain of the CsI layer, respectively. The factors related to the TFT array are the electronic noise S_n and the pixel width a_p . The denominator of Eq. (7) is the dose normalized NPS. The first term is the x-ray quantum noise, the second term is the secondary quantum noise associated with the variance in gain in the conversion and the avalanche process, and the third term is the contribution from the electronic noise of the TFT array. This expression shows that the electronic noise is more important at low dose, and is inversely proportional to g_{av}^2 . Therefore introducing avalanche gain is an effective method for reducing noise at low dose. The secondary quantum noise for $g_{av} \gg 1$ is approximately twice that for $g_{av}=1$, assuming η is the same in both cases. This excess secondary quantum noise is the penalty for avalanche gain. However for SHARP-AMFPI with high conversion gain g and efficient optical coupling between CsI and HARP, i.e., $g \eta_x \gamma \eta \gg 2$, the secondary quantum noise is negligible compared to the x-ray quantum noise. Hence the DQE of SHARP-AMFPI will not be degraded by the noise associated with avalanche gain. This has been demonstrated experimentally by coupling a HARP tube to the output of an x-ray image intensifier (XRII) and measuring the DQE as a function of avalanche gain g_{av} .²⁹ It was shown that DQE remains essentially constant as a function of g_{av} (with electronic noise negligible in all cases).

In a later investigation of the inherent imaging performance of CsI layers, we included the effect of K-fluorescence reabsorption of CsI in the cascaded linear system model for indirect AMFPI.³⁰ Our results showed that the K-fluorescence reabsorption in CsI has two effects: (1) degradation of the Swank factor for x-ray energies above the K edges and (2) additional image blur, which accounts for a

drop in presampling MTF of 20–30 % at 10 cycles/mm for CsI thickness between 150 and 600 μm . For the present paper, a more complete cascaded linear system model was developed that includes the effect of direct x-ray interaction in HARP. Shown in Fig. 6 are the serial and parallel cascaded stages involved in the formation of an x-ray image by SHARP-AMFPI. Each stage can be categorized as one of the following six processes: (1) gain or selection; (2) stochastic blurring; (3) deterministic blurring; (4) aliasing; (5) addition; and (6) parallel processes. There are two parallel processes: one associated with the probability of K-fluorescence generation and reabsorption in CsI, and the other with direct interaction of x rays in the HARP layer. We have previously described in detail the transfer of spatial frequency dependent signal $\Phi(f)$ and NPS, $S(f)$ through all the stages except direct x-ray interaction in the HARP layer. This process will be described in Sec. III C of this paper.

Using the cascaded linear system model shown in Figure 6, we investigated two important aspects of the x-ray imaging performance of SHARP-AMFPI. One is the pixel x-ray response of the detector, i.e., the linearity and dynamic range, for both the avalanche and nonavalanche operational modes; the other is the effect of direct x-ray interaction in HARP on the DQE of the detector. These will be described in Sections B and C, respectively.

B. Pixel x-ray response

In this section, we will apply the E_{Se} dependence of g_{av} and η derived previously in Sec. II B to the cascaded linear system model to determine the x-ray response of SHARP-AMFPI. Due to the difference in resolution and avalanche gain requirement for mammography and radiography/fluoroscopy (R/F), the calculation will be performed separately for these two imaging applications. From the cascaded linear system model the mean signal from each pixel of the detector is given by

TABLE I. SHARP-AMFPI detector design parameters and operating conditions chosen for different x-ray imaging applications.

	Mammography detector		R/F detector	
	Tomosynthesis	Screening	Fluoroscopy	Radiography
Pixel pitch a_p (μm)	70		200	
X-ray spectrum	28 kVp Mo/Mo, 4 cm PMMA		RQA5	
Electronic noise	2000 electrons		1500 electrons	
CsI (75% packing)	150 μm HR		600 μm HL	
W for CsI (eV)	30		18	
γ	0.8		0.8	
Minimum exposure	0.1 mR	1 mR	0.1 μR	30 μR
E_{Se} (V/μm)	110	105	110	95
η	0.36	0.35	0.36	0.31
g_{av}	46	12	46	2.3

$$\Phi_s = \frac{a_p^2 \gamma \eta g_{av} E_{ab}}{W}, \quad (8)$$

where W is the energy required to generate an optical photon in CsI, and E_{ab} is the x-ray energy absorbed by CsI per unit area. E_{ab} includes contributions from all three parallel paths associated with K-fluorescence

$$E_{ab} = \sum_E q_0(E) \eta_x(E) [(1 - P_k)E + (E - E_k)P_k + E_k P_k f_k], \quad (9)$$

where $q_0(E)$ is the incident x-ray photons per unit area as a function of energy E for a given x-ray spectrum, P_k is the probability of K fluorescence, E_k is the energy of the K-fluorescence photon, and f_k is the fraction of K fluorescence reabsorbed in the CsI layer. Each of the K-fluorescence related terms in Eq. (9) was determined separately for the K_α and K_β photons from both Cs and I atoms and integrated to obtain the final result of E_{ab} .

We have previously investigated the inherent x-ray imaging performance of CsI (Tl) using individual samples optimized for either high resolution (HR) or high light output (HL).³⁰ Our results showed that the HR type has essentially no depth dependent blur and as a result provides better DQE(f) at high spatial frequencies compared to HL CsI layers. This was achieved at the cost of a lower light output (60%) for the HR compared to the HL CsI. For the calculation in this paper, we used 150 μm HR CsI for mammography and 600 μm HL CsI for R/F applications. Our previously measured values for A_S , W , and presampling MTF of these CsI layers were used in the cascaded linear system model. Since we have not yet implemented the depth dependent blur of CsI in our cascaded linear system model, the DQE(f) at high frequencies for the 600 μm HL CsI layer (for R/F) will be overestimated. Table I summarizes the detector parameters and HARP operating conditions chosen for each application. For mammography, we consider two different image acquisition modes: screening mammography and tomosynthesis [where several images of the breast are acquired from different viewing angles for tomographic reconstruction of three-dimensional (3D) images].

1. Radiography/Fluoroscopy

Shown in Fig. 7(a) is the DQE(f) calculated using the cascaded linear system model for the detector with different g_{av} settings. For comparison we also calculated the DQE(f)

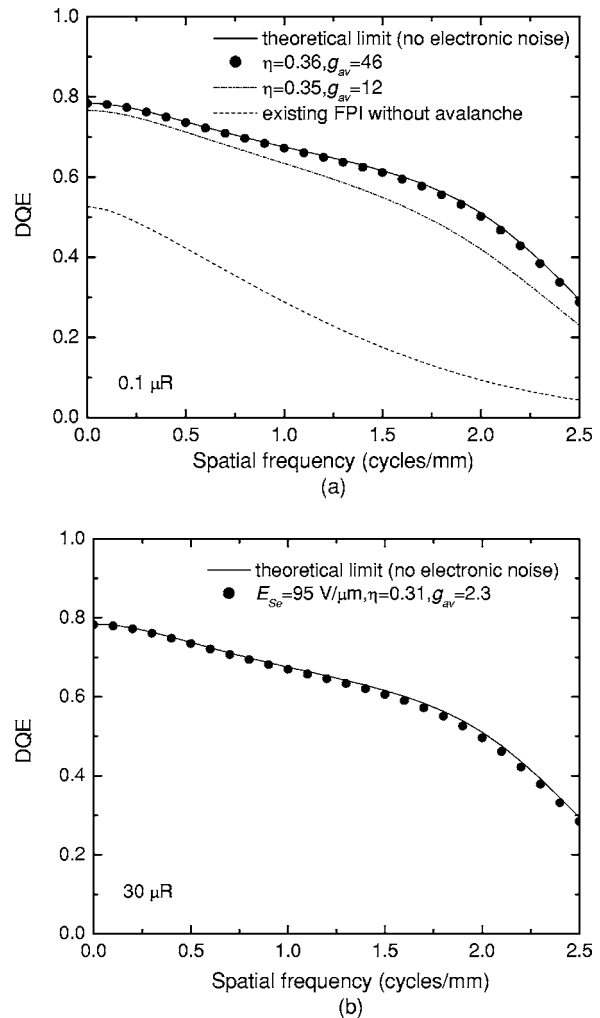


FIG. 7. Calculated DQE (f) using the detector parameters and operating conditions shown in Table I for a fluoroscopy detector at the x-ray exposure level of (a) 0.1 μR and (b) 30 μR.

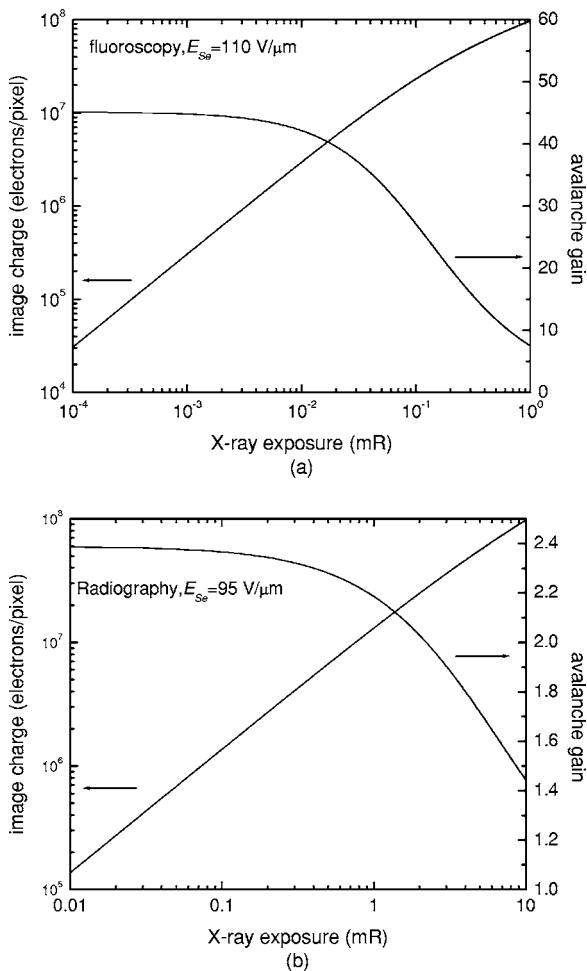


FIG. 8. Calculated image charge on each pixel of the detector and the corresponding avalanche gain as a function of x-ray exposure for the detector operational setting of (a) fluoroscopy and (b) radiography.

of existing indirect AMFPI technology without avalanche gain using $\eta=0.8$ [which is the quantum efficiency of *a*-Si PD (Ref. 1)] and an optimistic fill factor of unity. The calculation was performed for the lowest exposure in fluoroscopy ($0.1 \mu\text{R}$), where the detector performance is most susceptible to electronic noise. It shows that $g_{av}=46$ is sufficient to bring the DQE(f) to its theoretical limit (i.e., a detector without electronic noise). The DQE(f) for the next highest $g_{av}=12$ measured at $E_{Se}=105 \text{ V}/\mu\text{m}$ also provides reasonable DQE, which is a significant improvement from existing FPI technology. Thus an E_{Se} between 105 and $110 \text{ V}/\mu\text{m}$ will be adequate for fluoroscopy. Figure 7(b) shows the DQE(f) calculated for the lowest radiographic exposure of $30 \mu\text{R}$. It shows that $E_{Se}=95 \text{ V}/\mu\text{m}$ can provide sufficient η (0.31) and g_{av} (2.3). Hence the E_{Se} values chosen in Table I are adequate for the dual-mode operation of a R/F detector.

Shown in Fig. 8 are the calculated pixel x-ray responses for the R/F detector under two different operational conditions. Here we assumed that the dominant pixel capacitance is the capacitance of the HARP layer. This condition results in the largest drop in the potential across the HARP layer for a given x-ray exposure, and creates the biggest effect on

linearity. Figure 8(a) shows that for fluoroscopy, the initial $E_{Se}=110 \text{ V}/\mu\text{m}$ provides a g_{av} of 46. Within the regular exposure range of $0.1\text{--}10 \mu\text{R}$ per frame in fluoroscopy, the detector has good linearity, i.e., an essentially constant g_{av} . With further increase in exposure, which corresponds to the exposure near or beyond the edge of the human body, the x-ray response becomes sublinear with a decrease in g_{av} . This decrease in g_{av} ensures a wide dynamic range for the detector because there is no "hard" saturation. The pixel potential will continue to increase as a function of x-ray exposure until it reaches the predetermined V_{max} for high voltage protection of the TFTs. The method for high voltage protection was described in detail elsewhere.³¹ The pixel potential for the exposure of 1 mR in the fluoroscopy mode is $V_P=56 \text{ V}$, which is safe for properly designed *a*-Si TFTs.³² The mechanisms for high voltage damage for *a*-Si TFTs are most likely due to gate dielectric breakdown or heating.³³ In AMFPI, the readout of image charge usually results in an exponential decay of the TFT channel current, and is not likely to generate enough heating to cause damage. Hence the main mechanism for high voltage damage in AMFPI is gate dielectric breakdown. The breakdown voltage depends on the thickness and material properties of the gate insulator, which is usually silicon nitride with a thickness of several thousand angstroms.³⁴ Since silicon nitride films can stand an electric field of up to $10^3 \text{ V}/\mu\text{m}$, a pixel potential of up to 100 V may be safe for the TFTs. Figure 8(b) shows that with a much lower $g_{av}=2.3$ programmed for radiography, the detector response for the regular exposure range of $30 \mu\text{R}\text{--}3 \text{ mR}$ is essentially linear with very little change in g_{av} . Comparing Figures 8(a) and 8(b), the image charge on the pixel is in the same range despite their large difference in exposure range. This demonstrates the wide dynamic range (over five orders of magnitude) of the detector that is made possible by varying g_{av} for different x-ray imaging applications. This is an advantage over detectors with constant high gain, which have the problem of pixel saturation for radiographic applications.

2. Mammography

Figures 9(a) and 9(b) show the DQE calculated for mammography using the detector parameters and operating conditions listed in Table I for tomosynthesis and screening applications. Also shown in Fig. 9(a) is the calculated DQE of indirect FPI without avalanche gain ($\eta=0.8$ and unity fill factor), where the electronic noise causes severe degradation of DQE at the low dose for each view of tomosynthesis. Figure 9 shows that the choices of E_{Se} for both tomosynthesis and screening mammography modes are adequate to achieve the theoretical limit of DQE without electronic noise.

The pixel x-ray response for mammography was calculated using Eq. (8) and the results are shown in Figs. 10(a) and 10(b) for tomosynthesis and screening mammography, respectively. Two sets of curves are shown in each graph of Fig. 10, one without additional pixel storage capacitance, and the other with a storage capacitor of $C_{st}=0.5 \text{ pF}$. The mini-

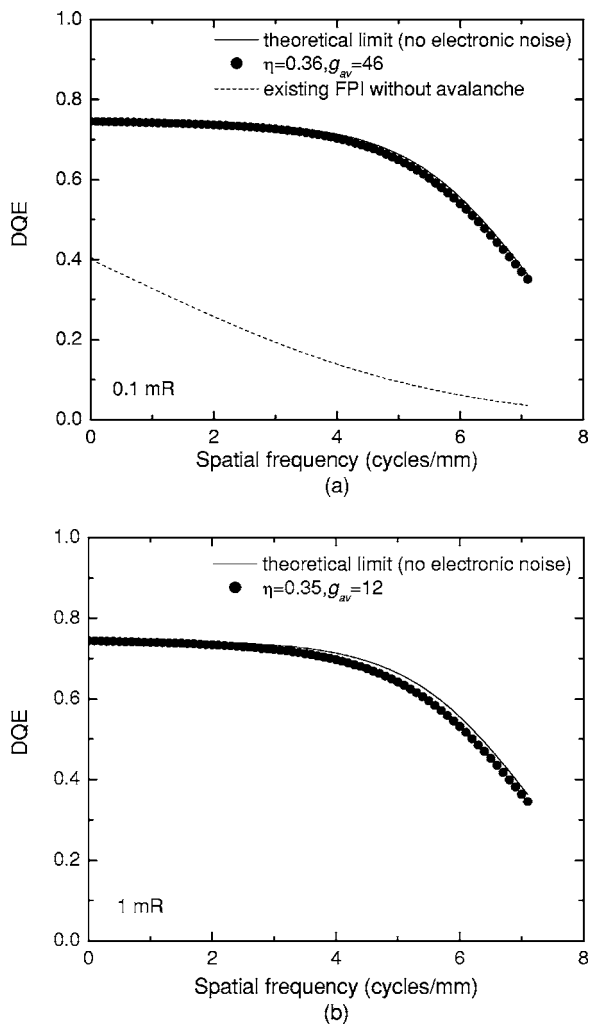


FIG. 9. Calculated DQE (f) using the detector parameters and operating conditions shown in Table I for mammography (a) tomosynthesis with minimum exposure of 0.1 mR and (b) screening with minimum exposure of 1 mR.

mum exposure in each graph of Fig. 10 corresponds to the detector exposure behind dense breast tissue, and the maximum corresponds to raw exposure. Figure 10 shows that when there is no additional storage capacitance, the signal increases sublinearly as a function of the x-ray exposure. This is because the pixel capacitance due to the HARP layer for mammography is only ~ 0.03 pF with $a_p = 70 \mu\text{m}$, which is much smaller than that for the R/F detector (0.28 pF). Hence the signal accumulated on each pixel creates a much more significant drop in E_{Se} , which causes a rapid decrease in g_{av} . The maximum image charge shown in Figs. 10(a) and 10(b) corresponds to a pixel potential of ~ 100 and 210 V, respectively. These potentials exceed the maximum safe voltage for the TFTs. One method for alleviating this problem while maintaining the same dynamic range is to add a pixel storage capacitance C_{st} . With $C_{st}=0.5$ pF, the pixel potential rises much more slowly and the x-ray response of the detector becomes more linear, as shown in Fig. 10. The pixel

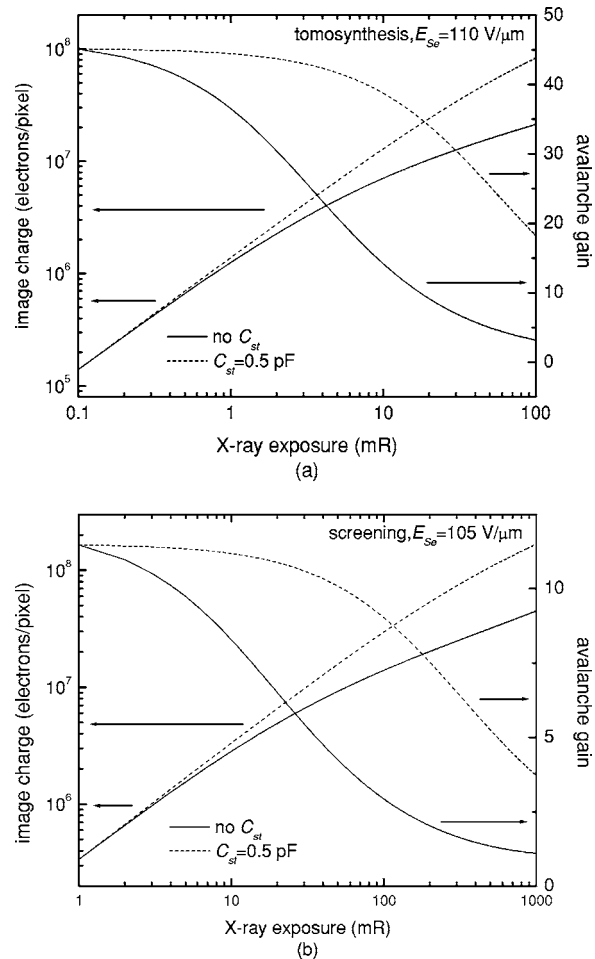


FIG. 10. Calculated image charge on each pixel of the mammography detector and the corresponding avalanche gain as a function of x-ray exposure with or without the addition of a pixel storage capacitor. The results are for detector operating conditions chosen for (a) tomosynthesis image acquisition and (b) screening mammography.

potential corresponding to the maximum exposures in Figs. 10(a) and 10(b) is only 25 and 50 V, respectively, both of which are safe for the TFTs.

C. Direct x-ray interaction in HARP

In indirect AMFPI using phosphor and a -Si photodiodes, direct interaction of x rays in the photodiodes produces additional noise.³⁵ This is because the x ray to charge conversion gain in the photodiodes is much higher (e.g., 45 times in the example of Ref. 35) than that in the phosphors, and therefore each direct interaction x ray produces much higher signal (and noise) than that absorbed in the phosphor. For our proposed detector, the HARP sensor (e.g., $d_{Se}=8 \mu\text{m}$) is much thicker than the a -Si photodiodes ($\sim 1 \mu\text{m}$) in existing indirect FPI, hence there will be more direct x-ray interaction events. Fortunately the x ray to charge conversion gain in HARP³⁶ ($W_{Se}=16 \text{ eV}$ at $E_{Se}=100 \text{ V}$) is very similar to that in CsI, thus direct x-ray interaction in HARP is not expected to add additional noise at low spatial frequencies. At high spatial frequencies, however, the effect of direct x-ray interaction could be more significant. This is because both the

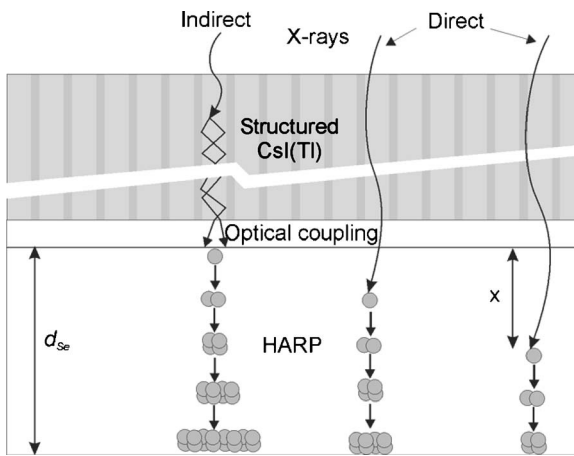


FIG. 11. Diagram showing the depth dependent gain for direct x-ray interaction in HARP. For the x rays absorbed in CsI, the light photons created enter the top interface of HARP, where holes are generated and undergo avalanche multiplication for the entire thickness of HARP d_{Se} . For the x rays interacting directly with HARP at depth x from the top interface, the holes generated undergo avalanche for the thickness of $(d_{Se} - x)$, which causes depth dependence avalanche gain variation.

signal and the NPS due to x rays absorbed in CsI decrease as a function of spatial frequency due to blur in CsI, whereas the signal and NPS due to direct x-ray interaction in HARP are essentially white (without including the effect of K fluorescence). Furthermore, when HARP is operated in the avalanche mode, the x rays absorbed by HARP will experience different avalanche gain depending on their depth of interaction. As shown in Fig. 11, x rays absorbed in HARP at a depth x from the top (light entrance) interface have an effective thickness for avalanche multiplication of $(d_{Se} - x)$. This could lead to a depth dependent variation in g_{av} , and add additional noise.³⁷ In the following we will derive the propagation of signal and noise due to direct x-ray interaction in HARP using the flow diagram shown in Fig. 6, and investigate its effect on the DQE of SHARP-AMFPI.

1. Signal and noise propagation for direct x-ray interaction

As shown in Fig. 6, the input to the parallel path for direct x-ray interaction in HARP is the x rays transmitted through the CsI layer q_1 , which is a function of x-ray energy. For clarity we assume a monoenergetic x-ray beam in the following derivation of theory, although we used the full x-ray spectrum in our calculation of direct x-ray interaction. We ignored the effect of K-fluorescence reabsorption in HARP. Under this assumption, both the signal and NPS for direct x-ray interaction are white prior to the pixel aperture function, hence we could omit the frequency dependence in the following derivation. The x-ray signal produced at depth x into the HARP layer by a small thickness dx of $a\text{-Se}$ is given by

$$\Phi(x) = q_1 e^{-\mu x} g_{av}(x) g_{Se} \mu dx, \quad (10)$$

where μ is the linear attenuation coefficient of $a\text{-Se}$, and g_{Se} is the average x ray to charge conversion gain which is equal

to E/W_{Se} . The depth dependence in g_{av} can be derived from Eq. (4) as $g_{av}(x) = \exp[\beta(d_{Se} - x)]$. The NPS due to direct interaction as a function of depth $S(x)$ is given by³⁷

$$S(x) = q_1 e^{-\mu x} [(g_{Se}^2 + \sigma_{g_{Se}}^2) g_{av}^2(x) + g_{Se} \sigma_{g_{av}}^2(x)] \mu dx. \quad (11)$$

Integrating both Eqs. (10) and (11) with respect to x from 0 to d_{Se} , we obtain the total signal and NPS due to direct x-ray interaction

$$\Phi = \frac{q_1 \mu g_{Se} (e^{\beta d_{Se}} - e^{-\mu d_{Se}})}{\mu + \beta} \quad (12)$$

and

$$S = \frac{q_1 \mu (g_{Se}^2 + \sigma_{g_{Se}}^2) (e^{2\beta d_{Se}} - e^{-2\mu d_{Se}})}{\mu + 2\beta}. \quad (13)$$

2. Calculation results

Using Eqs. (12) and (13), we calculated the contribution to the total signal and NPS by the direct interaction of x rays in HARP using the parameters shown in Table I for a R/F detector. With a RQA5 x-ray spectrum and a $600\text{ }\mu\text{m}$ HL layer of CsI, the fraction of x rays transmitted through the CsI layer is 13.2%, out of which $\sim 1\%$ is absorbed by the HARP layer. Shown in Fig. 12(a) is a comparison between the presampling signal spectra (before the pixel aperture function) due to x rays absorbed in CsI and direct x-ray interaction in HARP. At low frequencies, the signal due to direct x-ray interaction is less than 0.2% of that due to x-ray absorbed in CsI. This is consistent with the difference in x-ray quantum efficiency between CsI and HARP. At high frequencies (e.g., 5 cycles/mm), the signal from CsI decreases due to the blur in CsI, however the signal from direct x-ray interaction in HARP stays constant. But the latter is still negligible. Shown in Fig. 12(b) is the NPS (before pixel aperture function) comparison. At 5 cycles/mm, the NPS due to direct x-ray interaction becomes significant ($\sim 17\%$ of the NPS due to CsI). However below the Nyquist frequency of 2.5 cycles/mm, it is still negligible ($< 3\%$). This is why there is no significant change in DQE after including the direct x-ray interaction events in HARP, as shown in Fig. 13. Therefore we can conclude that direct x-ray interaction in HARP in an indirect FPI with avalanche gain has no degradation effect on DQE of the detector.

IV. EFFECT OF HARP THICKNESS UNIFORMITY

An important issue for making a large area HARP is its thickness uniformity. Currently HARP films can be made very uniform for an area of 1–2 in. in diameter with essentially no visible gain variation in the images. The images currently produced by HARP for broadcast applications do not require any gain uniformity correction. The area of HARP needs to be increased significantly for x-ray imaging applications. Uniform, large area $a\text{-Se}$ films have already been developed for direct FPI, however the uniformity requirement for HARP in indirect FPI with avalanche gain is expected to be much higher. In this section we will derive the

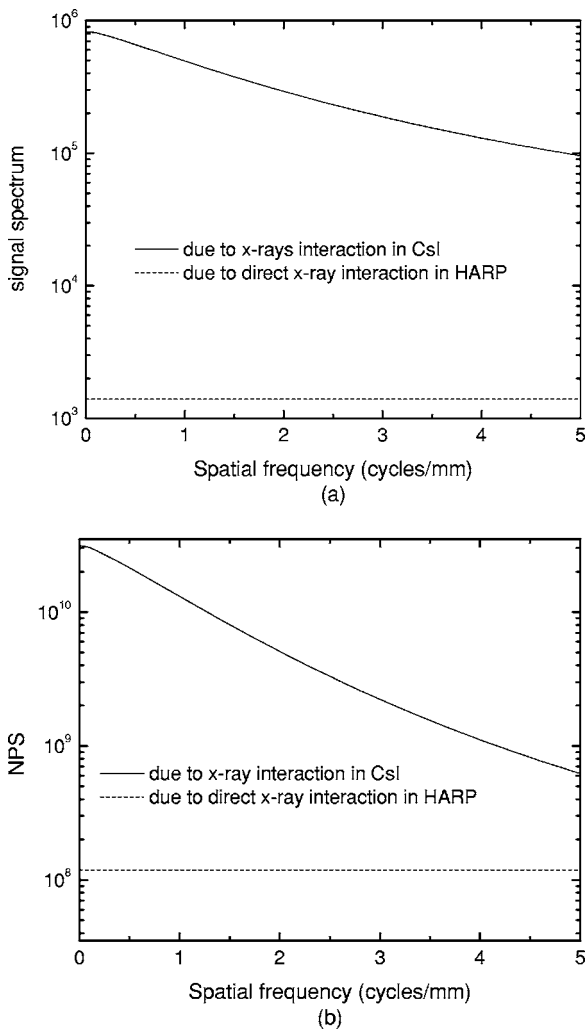


FIG. 12. Comparison of the presampling signal and NPS (before pixel aperture function) due to x ray absorbed in CsI and direct x-ray interaction in HARP: (a) signal spectra, where the signal due to direct interaction is negligible and (b) NPS, where the NPS due to direct interaction under the Nyquist frequency of 2.5 cycles/mm is negligible.

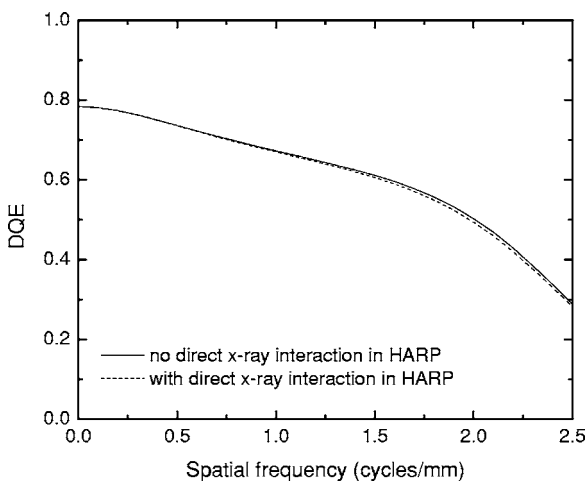


FIG. 13. Comparison between the DQE of SHARP-AMFPI with and without consideration of direct x-ray interaction in HARP.

relationship between thickness nonuniformity and gain nonuniformity for HARP sensors so that the results can be used as a guideline for engineering of large area HARP layers for FPI.

A. Relationship between HARP avalanche gain and thickness uniformity

During the operation of HARP, a constant potential V_b is applied to the top ITO bias electrode, as shown in Fig. 1(b). After each image readout, the TFT array resets the potential on pixel electrodes to $V_p=0$ V. A nonuniformity in the thickness of HARP will result in a variation in E_{Se} and hence a spatial nonuniformity in gain. An increase in d_{Se} under a constant V_b causes a decrease in E_{Se} . Although on one hand an increase in d_{Se} tends to increase g_{av} [Eq. (4)], it also results in a simultaneous decrease in E_{Se} under a constant V_b . The overall effect is a decrease in g_{av} because of its additional exponential dependence on E_{Se} shown in Eq. (5). By substituting $E_{Se}=V_b/d_{Se}$ into Eq. (6) and differentiating both sides, we obtain

$$\frac{1}{\ln g_{av}} \frac{\Delta g_{av}}{g_{av}} = \frac{\Delta d_{Se}}{d_{Se}} - \frac{\beta_2}{V_b} \Delta d_{Se}. \quad (14)$$

Equation (14) can be rewritten as

$$\frac{\Delta g_{av}}{g_{av}} = \ln(g_{av}) \left(1 - \frac{\beta_2}{E_{Se}} \right) \frac{\Delta d_{Se}}{d_{Se}}. \quad (15)$$

Equation (15) shows that with $\beta_2 > E_{Se}$, which is true for HARP, a positive change in d_{Se} results in a negative change in g_{av} . Equation (15) also shows that the percentage variation in avalanche gain is proportional to $\ln(g_{av})$ and the percentage thickness variation, hence HARP layers operated with higher g_{av} are more susceptible to gain nonuniformity caused by thickness nonuniformity.

B. Calculation of gain nonuniformity

Using Eqs. (4) and (5), and the values for β_1 and β_2 determined in Sec. II, the variations in g_{av} were calculated for both positive and negative change in d_{Se} around 8 μ m, and results are shown in Fig. 14. Three V_b values of 840, 864, and 880 V were used, which corresponds to g_{av} of 12, 25, and 46, respectively. Figure 14 shows that the slope of the curve, i.e., percentage change in g_{av} , is much higher for negative change in d_{Se} , which causes an increase in g_{av} , than it is for positive. Hence when choosing the bias potential V_b of HARP for a desired E_{Se} , the smallest d_{Se} for the entire detector area should be used, so that the variation in thickness is positive from the reference thickness. If we assume the smallest $d_{Se}=8$ μ m, the percentage changes in g_{av} due to an increase in d_{Se} of 1% are 19, 23, and 26 %, respectively, for the three V_b settings of 840, 864, and 880 V. The change in g_{av} increases to 33, 40, and 44 %, respectively, when the variation in d_{Se} increases to 2%. This range of g_{av} nonuniformity is certainly within the capability of gain correction and the dynamic range of the electronic circuits of FPI. With a further increase in d_{Se} to 4%, the value for g_{av} will decrease

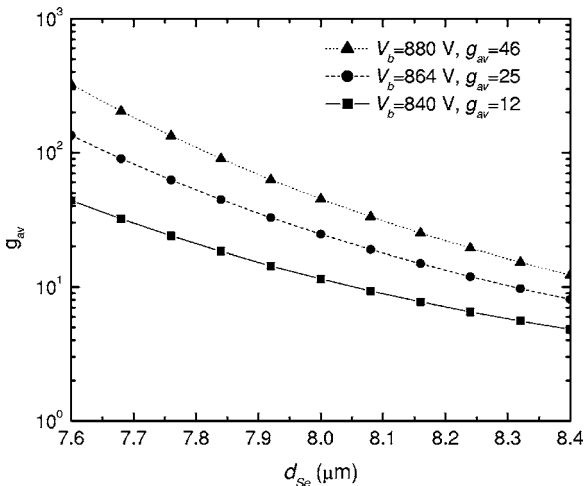


FIG. 14. Avalanche gain g_{av} calculated as a function of the thickness of HARP, which varies around 8 μm , under a constant bias potential V_b of 840, 864, and 880 V.

from the original setting of 46, 25, and 12 to 15, 10, and 6, respectively, which is a gain nonuniformity of two to three folds. Although the variation in g_{av} is significant, it is not expected to cause significant degradation in the DQE performance, as can be seen in the example of $g_{av}=46$ and 12 shown in Fig. 7(a). However this will pose a greater challenge for the uniformity correction algorithm. Hence we can conclude that a thickness nonuniformity of 2% is desirable for a HARP layer, and 4% nonuniformity could still possibly be tolerated.

V. CONCLUSIONS

The feasibility of a concept of indirect conversion flat-panel detector with avalanche gain is being investigated. The avalanche gain and quantum efficiency of an 8 μm thick HARP layer were investigated experimentally as function of E_{Se} . These characteristics of HARP were applied to a cascaded linear system to determine the optimal operating conditions required for x-ray imaging. Our results showed that by varying the avalanche gain between 2 and 46, x-ray quantum noise limited performance and a wide dynamic range can be obtained for both R/F and mammographic imaging applications. Direct x-ray interaction in HARP was shown not to affect the imaging performance. Due to the rapid increase in g_{av} as a function of E_{Se} , a small variation in d_{Se} can cause significant nonuniformity in avalanche gain. It is necessary to keep the thickness uniformity of a HARP layer within 4%, which could maintain a high DQE across the entire detector and make the variation in g_{av} correctable using gain calibration.

ACKNOWLEDGMENTS

We gratefully acknowledge financial support from the NIH (1 R01 EB002655-01) and the U.S. Army Breast Cancer Research Program (W81XWH-04-1-0554).

^{a)}Electronic mail: wei.zhao@sunysb.edu

¹J. A. Rowlands and J. Yorkston, "Flat panel detectors for digital radiography," in *Medical Imaging, Volume 1, Physics and Psychophysics, Psychophysics*, edited by J. Beutel, H. L. Kundel, and R. L. Van Metter (SPIE, Bellingham, 2000), pp. 223–328.

²X. Liu and C. C. Shaw, " α -Si:H/CsI(Tl) flat-panel versus computed radiography for chest imaging applications: Image quality metrics measurement," *Med. Phys.* **31**, 98–110 (2004).

³P. Monnin, D. Gutierrez, S. Bulling, D. Lepori, J.-F. Valley, and F. R. Verdun, "Performance comparison of an active matrix flat panel imager, computed radiography system, and a screen-film system at four standard radiation qualities," *Med. Phys.* **32**, 343–350 (2005).

⁴Wei Zhao and J. A. Rowlands, "Digital radiology using active matrix readout of amorphous selenium: Theoretical analysis of detective quantum efficiency," *Med. Phys.* **24**, 1819–1833 (1997).

⁵L. E. Antonuk, K.-W. Jee, Y. El-Mohri, M. Maolinby, S. Nassif, X. Rong, Q. Zhao, J. H. Siewerdsen, R. A. Street, and K. S. Shah, "Strategies to improve the signal and noise performance of active matrix, flat-panel imagers for diagnostic x-ray applications," *Med. Phys.* **27**, 289–306 (2000).

⁶J. H. Siewerdsen and D. A. Jaffray, "A ghost story: Spatio-temporal response characteristics of an indirect-detection flat-panel imager," *Med. Phys.* **26**, 1624–1641 (1999).

⁷M. Overdick, T. Solf and H. Wischmann, "Temporal artifacts in flat dynamic x-ray detectors," *Proc. SPIE* **4320**, 47–58 (2001).

⁸L. T. Niklason *et al.*, "Digital tomosynthesis in breast imaging," *Radiology* **205**, 399–406 (1997).

⁹D. A. Jaffery and J. H. Siewerdsen, "Cone-beam computed tomography with a flat-panel imager: Initial performance characterization," *Med. Phys.* **27**, 1311–1323 (2000).

¹⁰Biao Chen and Ruola Ning, "Cone-beam volume CT breast imaging: Feasibility study," *Med. Phys.* **29**, 755–770 (2002).

¹¹A. Koch, J.-M. Macherel, T. Wirth, P. de Groot, T. Ducourant, D. Couder, J.-P. Moy, and E. Calais, "Detective quantum efficiency of an x-ray image intensifier chain as a benchmark for amorphous silicon flat panel detectors," *Proc. SPIE* **4320**, 115–120 (2001).

¹²S. Vedantham, A. Karella, S. Suryanarayanan, D. Albagli, S. Han, E. J. Tkaczyk, C. E. Landberg, P. R. Granfors, I. Levis, C. J. D'Orsi, and R. E. Hendrick, "Full breast digital mammography with an amorphous silicon-based flat-panel detector: Physical characteristics of a clinical prototype," *Med. Phys.* **27**, 558–567 (2000).

¹³Wei Zhao, W. G. Ji, Anne DeBrie, and J. A. Rowlands, "Imaging performance of amorphous selenium based flat-panel detectors for digital mammography: Characterization of a small area prototype detector," *Med. Phys.* **30**, 254–263 (2003).

¹⁴R. A. Street, S. E. Ready, K. Van Schuylenbergh, J. Ho, J. B. Boyce, P. Nylen, K. Shah, L. Melekhov, and H. Hermon, "Comparison of PbI₂ and HgI₂ for direct detection active matrix x-ray image sensors," *J. Appl. Phys.* **91**, 3345–3355 (2002).

¹⁵M. Zahangir Kabir and S. O. Kasap, "Charge collection and absorption-limited sensitivity of x-ray photoconductors: Applications to α -Se and HgI₂," *Appl. Phys. Lett.* **80**, 1664–1666 (2002).

¹⁶N. Matsuura, Wei Zhao, Z. Huang, and J. A. Rowlands, "Digital radiology using active matrix readout: Amplified pixels for fluoroscopy," *Med. Phys.* **26**, 672–681 (1999).

¹⁷K. S. Karim, Y. K. Vygranenko, D. A. Striakhilev, A. Nathan, S. Germann, J. A. Rowlands, G. Belev, C. Koughia, R. Johanson, and S. O. Kasap, "Active pixel image sensor for large-area medical imaging," *Proc. SPIE* **5030**, 38–47 (2003).

¹⁸J. P. Lu, K. Van Schuylenbergh, J. Ho, Y. Wang, J. B. Boyce, and R. A. Street, "Flat panel imagers with pixel level amplifiers based on polycrystalline silicon thin-film transistor technology," *Appl. Phys. Lett.* **80**, 4656–4658 (2002).

¹⁹K. Tanioka, J. Yamazaki, K. Shidara, K. Taketoshi, T. Kawamura, T. Hirai, and Y. Takasaki, "Avalanche-mode amorphous selenium photoconductive target camera tube," *Adv. Electron. Electron Phys.* **74**, 379–387 (1988).

²⁰H. M. Rougeot and G. E. Possin, "Radiation image detector with optical gain selenium photosensors," U. S. Patent No. 5,198,673.

²¹A. Jean, L. Laperriere, A. Legros, H. Mani, Z. Shukri, and H. Rougeot, "New cesium iodide-selenium x-ray detector structure for digital radiography and fluoroscopy," *Proc. SPIE* **3659**, 298–306 (1999).

²²T. Ohshima, K. Tsuji, K. Sameshima, T. Hirai, K. Shidara, and K. Take-

- toshi, "Excess noise in amorphous selenium avalanche photodiodes," *Jpn. J. Appl. Phys., Part 2* **30**, L1071–L1074 (1991).
- ²³Wei Zhao, D. C. Hunt, Kenkichi Tanioka, and J. A. Rowlands, "Indirect flat-panel detectors with avalanche gain," *Proc. SPIE* **5368**, 150–161 (2004).
- ²⁴M. Kubota, T. Kato, S. Suzuki, H. Maruyama, K. Shidara, K. Tanioka, K. Sameshima, T. Makishima, K. Tsuji, T. Hirai, and T. Yoshida, "Ultrahigh-sensitivity new super-HARP camera," *IEEE Trans. Broadcasting*, **42**, 251–258 (1996).
- ²⁵D. M. Pai and R. C. Enck, "Onsager mechanism of photogeneration in amorphous selenium," *Phys. Rev. B* **11**, 5163–5174 (1975).
- ²⁶K. Tsuji, Y. Takasaki, T. Hiri, J. Yamazaki, and K. Tanioka, "Avalanche phenomenon in amorphous selenium," *Optoelectron., Devices Technol.* **9**, 367–378 (1994).
- ²⁷R. J. McIntyre, "Multiplication noise in uniform avalanche diodes," *IEEE Trans. Electron Devices* **13**, 164–168 (1966).
- ²⁸S. M. Sze, *Physics of Semiconductor Devices*, 2nd ed. (Wiley, New York, 1981).
- ²⁹D. C. Hunt, Wei Zhao, and J. A. Rowlands, "X-ray imaging using amorphous selenium: Excess avalanche multiplication noise in indirect flat-panel detectors" (unpublished).
- ³⁰Wei Zhao, Goran Ristic, and J. A. Rowlands, "Inherent imaging performance of cesium iodide scintillators," *Med. Phys.* **31**, 2594–2605 (2004).
- ³¹Wei Zhao, J. Law, D. Waechter, Z. Huang, and J. A. Rowlands, "Digital radiology using active matrix readout of amorphous selenium: Detectors with high voltage protection," *Med. Phys.* **25**, 539–549 (1998).
- ³²Larry Antonuk, "*a-Si:H TFT-based active matrix flat-panel imagers for medical x-ray applications*," *Thin Film Transistor Materials and Processes Vol. 1: Amorphous Silicon Thin Film Transistors*, edited by Yue Kuo (Kluwer Academic Publishers, New York, 2004), pp. 395–482.
- ³³R. A. Martin, V. M. Da Costa, M. Hack, and J. G. Shaw, "High-voltage amorphous silicon thin-film transistors," *IEEE Trans. Electron Devices* **40**, 634–644 (1993).
- ³⁴Toshihisa Tsukada, "Active-matrix liquid-crystal displays," *Technology and Applications of Amorphous Silicon*, edited by Robert A. Street (Springer, New York, 2000), pp. 7–89.
- ³⁵A. Koch, "Influence of optical gaps on signal and noise properties of luminescent screen x-ray detectors," *Proc. SPIE* **5368**, 221–225 (2004).
- ³⁶D. C. Hunt, S. S. Kirby, and J. A. Rowlands, "X-ray imaging with amorphous selenium: X-ray to charge conversion gain and avalanche multiplication," *Med. Phys.* **29**, 2464–2471 (2002).
- ³⁷D. C. Hunt, B. Lui, and J. A. Rowlands, "An experimentally validated theoretical model of avalanche multiplication x-ray noise in amorphous selenium," *Proc. SPIE* **3977**, 106–116 (2000).

Screen optics effects on detective quantum efficiency in digital radiography: Zero-frequency effects

A. R. Lubinsky^{a)} and Wei Zhao

Department of Radiology, State University of New York at Stony Brook Stony Brook, New York 11794-8460

Goran Ristic and J. A. Rowlands

Imaging Research, Sunnybrook and Women's College Health Sciences Center Toronto,
Ontario M4N 3M5, Canada

(Received 6 October 2005; revised 30 December 2005; accepted for publication 17 February 2006;
published 28 April 2006)

Indirect flat panel imagers have been developed for digital radiography, fluoroscopy and mammography, and are now in clinical use. Screens made from columnar structured cesium iodide (CsI) scintillators doped with thallium have been used extensively in these detectors. The purpose of this article is to investigate the effect of screen optics, e.g., light escape efficiency versus depth, on gain fluctuation noise, expressed as the Swank factor. Our goal is to obtain results useful in optimizing screens for digital radiography systems. Experimental measurements from structured CsI samples were used to derive their screen optics properties, and the same methods can also be applied to powder screens. CsI screens, all of the same thickness but with different optical designs and manufacturing techniques, were obtained from Hamamatsu Photonics Corporation. The pulse height spectra (PHS) of the screens were measured at different x-ray energies. A theoretical model was developed for the light escape efficiency and a method for deriving light escape efficiency versus depth from experimental PHS measurements was implemented and applied to the CsI screens. The results showed that the light escape efficiency varies essentially linearly as a function of depth in the CsI samples, and that the magnitude of variation is relatively small, leading to a high Swank factor. © 2006 American Association of Physicists in Medicine. [DOI: 10.1118/1.2188082]

Key words: indirect detection, flat-panel detectors, digital radiography, cesium iodide, Swank factor

I. INTRODUCTION

Indirect flat panel imagers (FPI) have been developed for digital radiography (DR), fluoroscopy, and mammography, and are now in clinical use. These imagers use a scintillating x-ray screen as the primary x-ray detector and read the optical signal electronically with a large area active matrix array with an amorphous silicon (*a*-Si) photodiode and a switching thin film transistor at each pixel. Although powdered phosphor screens, like those used for many years in conventional screen/film radiography have been employed,¹ structured (needle-like) screens using cesium iodide (CsI) are more widely used in FPI. The CsI used in FPI are doped with thallium (Tl), which is different from the sodium (Na) doped CsI used in image intensifiers.²

Because in DR the detection, processing, and display functions are independent, they can be optimized separately. The detective quantum efficiency (DQE) has been used as the fundamental image quality metric for comparison between and optimization of DR detectors. Both theoretical modeling and experimental characterization of DQE have been performed for both direct³ and indirect⁴ FPI. Different types and thicknesses of screens have been used in indirect FPI for different x-ray imaging applications. It is important to understand and quantify the tradeoffs between x-ray absorption efficiency and resolution of different screen designs

and their effects on DQE. The effect of the screen component of a DR detector on the DQE has received attention recently for both powder⁵ and structured⁶ screens.

The study of the optical properties of x-ray screens predates their use in modern digital systems. A classic work by Swank⁷ quantified the effect of variability in the size of the scintillation pulses on DQE. This variability is called gain fluctuation noise, or "Swank noise." Swank also calculated the blurring effect of light scattering and the light escape efficiency in a turbid (light scattering) x-ray screen,⁸ making use of previous work by Marshak *et al.*,⁹ who was studying neutron diffusion, and by Hamaker,¹⁰ who had calculated the light emitted from a layer of x-ray fluorescent material. Hamaker had used the well known multiple light scattering theory of Kubelka and Munk,¹¹ which in turn was based on the equations developed by Schuster¹² for light propagation in stellar atmospheres.

In this article, we extend some of the previous work to investigate the effect of screen optics, e.g., light escape efficiency versus depth, on Swank factor, which is proportional to DQE of the detector at zero spatial frequency. Our goal is to obtain results useful in optimizing screens for DR systems. As an example, experimental measurements from structured CsI phosphors were used to derive their screen optics properties, but the same methods can be applied to powder screens.

II. THEORY AND BACKGROUND FOR SCREEN OPTICS

A. Escape efficiency (e)

In a phosphor screen, not all light photons generated by x rays escape the screen to contribute to signal. As shown in Fig. 1, we assume that the x-ray photons enter through the backing of the screen, and an optical sensor is placed next to the front surface. We assume that a number m of photons are created in the phosphor layer of the screen, either by prompt luminescence after x-ray absorption in a DR screen, or by stimulated luminescence in a computed radiography (CR) screen. In a nontransparent screen, these photons will scatter

from discontinuities in the optical index of refraction in the material, and may also be absorbed in the bulk or the backing of the screen. On average, n photons will make their way to the front (exit) surface, where the optical sensor is placed, and escape. We call the fraction n/m the escape efficiency or e . It depends on the thickness, reflectance of both surfaces and optical properties of the screen, and on the depth of creation of the original photons. Lubinsky *et al.*¹³ developed an explicit formula for the escape efficiency, e , of an isotropic powder screen in the context of a systems model for CR, using the Kubelka-Munk theory and summing multiple scattering terms

$$e(z, L, S, K, Rt, Rb) = \left(\frac{1 - Rt}{2} \right) \left\{ \frac{b(1 + Rb)\cosh[bS(L - z)] + (1 - Rb)(1 + a)\sinh[bS(L - z)]}{b(1 - RtRb)\cosh(bSL) + [a(1 + RtRb) - (Rt + Rb)]\sinh(bSL)} \right\}, \quad (1)$$

where z is the depth of light generation with $z=0$ representing the light exit side of the screen, L is the thickness of the screen, S and K are the scattering and absorption coefficients in the Kubelka-Munk theory, Rt and Rb are the reflectances at the top and bottom surfaces, and a and b are defined as $a=1+K/S$, $b=\sqrt{a^2-1}$, respectively. It should be noted that the optical coefficients S and K do not bear a simple relationship to the intrinsic optical constants of the screen medium or the physical parameters such as the particle size, as is pointed out in a recent paper on the interpretation of these parameters.¹⁴ It is not the intention of our present work to derive the values of S and K , but rather to deduce the escape efficiency from experimental characterization of the screen.

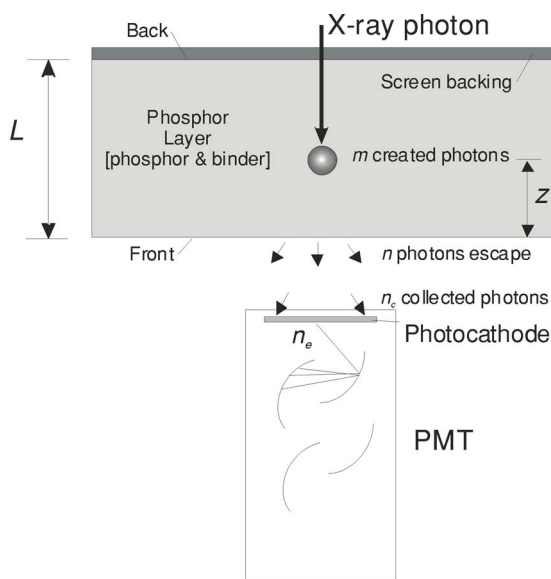


Fig. 1. Illustrating the creation and escape of photons from a scattering medium.

The escape efficiency model given in Eq. (1) can be used to study the effects of screen optics design. Figure 2 shows examples of e , calculated as a function of depth of light generation using Eq. (1), for different screen optics designs. We refer to the graph of escape efficiency e versus depth z as the e - z curve. In Fig. 2(a), the light absorption coefficient in the bulk of the screen is varied, and the e - z curve is plotted for a highly scattering material, with perfectly nonreflecting boundary conditions at both surfaces of the screen (back and front). The e is seen to vary strongly with depth, and as the absorption is increased, the decrease in e as a function of z becomes more rapid. Thus, although adding bulk absorption to a screen will limit the extent of spatial light spreading, which improves the MTF, it will also reduce the depth from which optical signal can propagate to the optical detector, thus reducing the noise-effective thickness of the screen. In Fig. 2(b), the reflectance of the screen backing is varied. It is noted that even a backing reflectance as high as 90%, is not very effective in boosting e for x rays absorbed near the backing. This is because in a highly scattering medium, a photon created near the back has typically a lot more than one chance to be absorbed as it diffuses near the back reflector. In order to appreciably improve e , the backreflectance must be near unity. Finally, in Fig. 2(c), the front (exit) surface reflectance is varied. A nonzero exit surface reflectance might occur due to internal reflection at the boundary when the optical coupling between the exit surface and the detector is imperfect. Here e is roughly linear within the bulk of the screen, but lower than unity at all depths due to internal reflection and absorption losses.

B. Swank factor and pulse height spectrum

The zero spatial frequency, or large area limit of the DQE, $DQE(0)$, for a radiographic screen is given by

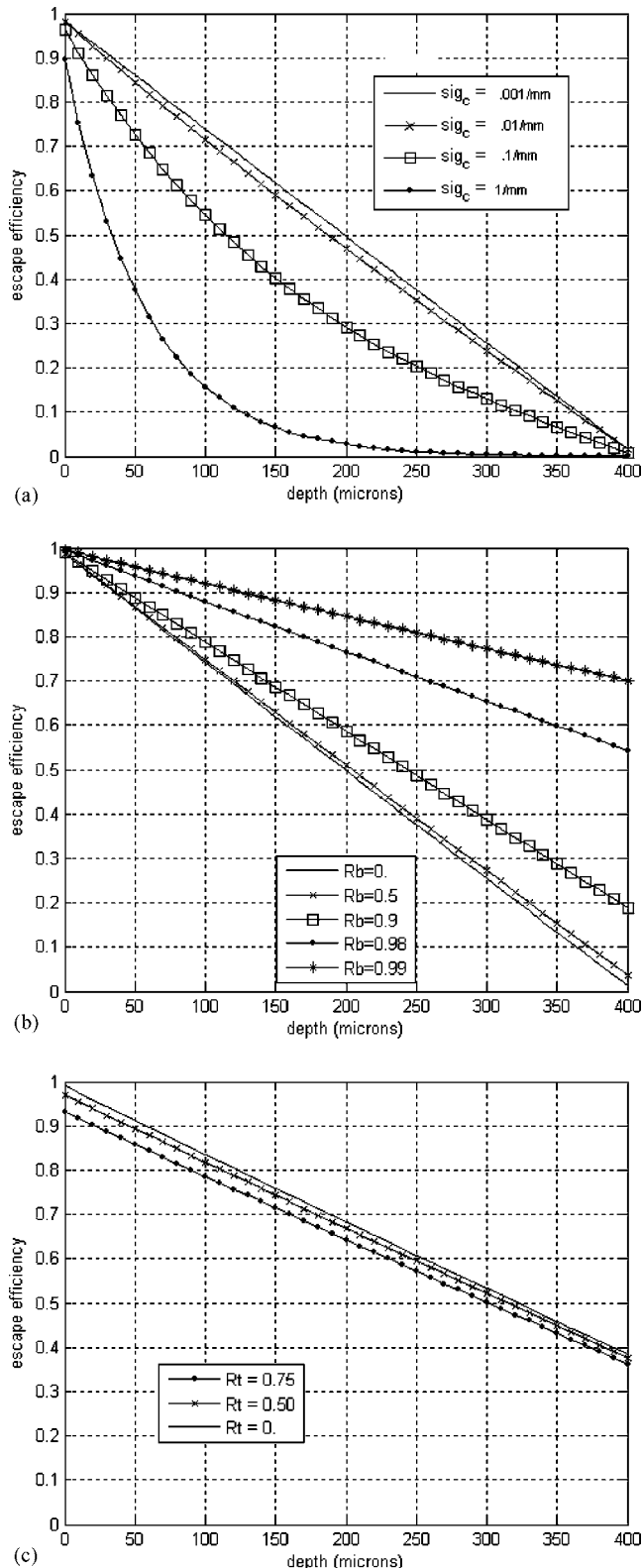


Fig. 2. (a) Escape efficiency vs depth. Scattering coefficient=100/mm. Top and bottom reflectance=0. Absorption coefficient varied: 0.001, 0.01, 0.1, 1.0/mm. (b) Escape efficiency vs depth. Scattering coefficient=100/mm. Absorption coefficients=0.001/mm. Top reflectance=0. Bottom reflectance varied: 0, 0.5, 0.9, 0.98, 0.99. (c) Escape efficiency vs depth. Scattering coefficient=100/mm. Absorption coefficient=0.001/mm. Bottom reflectance=0.95. Top reflectance varied: 0, 0.75, 0.5.

$$\text{DQE}(0) = \eta A_S, \quad (2)$$

where η is the x-ray absorption efficiency and A_S is the scintillation efficiency of the screen (which is often referred to as the Swank factor, and sometimes also denoted I). In an integrating detector, A_S arises because the size of the optical pulses produced by absorbed x rays is not a delta function but has a distribution. (In a detector with photon counting capability, the noise factor A_S due to varying pulse sizes is absent.) Swank⁷ decomposed the optical pulse distribution into components due to variations in optical propagation (OPD), variations in absorbed energy (AED), and the energy span of the incident x-ray spectrum. A_S can be expressed in terms of moments of the scintillation spectrum, i.e., the probability distribution function of the size of the optical pulses resulting from each x-ray interaction, as

$$A_S = \frac{M_1^2}{M_2 M_0}. \quad (3)$$

Swank⁷ showed that for monoenergetic x rays, and under certain reasonable conditions for the optical pulse distribution (OPD),

$$A_S = I_{\text{OPD}} I_{\text{AED}}. \quad (4)$$

We refer to the *measured* scintillation spectrum, using monoenergetic incident x rays, as the pulse height spectrum (PHS). The PHS has been measured for a variety of practical x-ray screens using photon counting,^{15,16} pulse shaping and multichannel pulse height analysis,¹⁷ and by synchronous detection of a chopped x-ray source.¹⁸ It has previously been shown experimentally that A_S is essentially constant with energy below the K edge of the screen, and drops to a minimum just above the K edge, due to the escape of characteristic K fluorescence.¹⁷

Below the K edge, and for monoenergetic x rays, most of the variation observed in the measured PHS is due to variations in e from various depths of creation in the x-ray screen. By measuring the PHS, we obtain experimental information that can potentially be used to estimate the variation of e with depth in the scintillating screen material.

III. MATERIAL AND METHODS

A. Material

We have investigated the inherent imaging performance of CsI with different thicknesses and types for optimization of indirect FPI with and without avalanche gain.¹⁹ Here we included the two 150 μm thick screens from the previous study and added two new screens of the same thickness but with entirely different manufacturing technique. All samples were manufactured by, and are available commercially from Hamamatsu Photonics Corporation. Aside from the difference in substrate materials and treatment of the surfaces, the intrinsic CsI material properties (e.g., doping) is the same for all samples. As shown in Fig. 3, the previous two CsI layers were deposited on fiber optic faceplate (FOP), with metallic and protective coating deposited on top of CsI. These layers were called fiber optic scintillator (FOS). During x-ray expo-

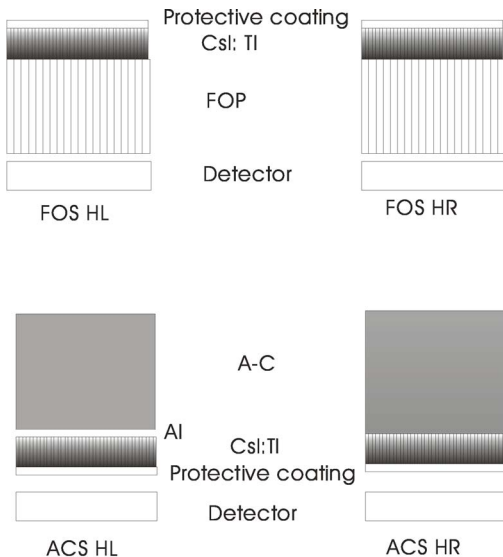


FIG. 3. Diagram illustrating four screen samples.

sure, the protective coating side of the CsI layer faced the x-ray source, and the FOP side was coupled to an optical sensor, e.g., a photomultiplier tube (PMT). Two types of 150 μm FOS were used in our experiment, one optimized for high light (HL) output, and the other optimized for high resolution (HR). Both HR and HL layers had metallic backing, but the HR type had different bulk material properties to minimize light spreading between columns, which improved resolution at the cost of lower light output (60% of that for HL). The two new samples added for the present study had the CsI deposited on amorphous carbon ($a\text{-C}$) substrate, hence, called amorphous carbon scintillator (ACS). They also came with HR and HL types. Compared to the HR, the HL layer had an additional aluminum reflective coating on the $a\text{-C}$ substrate before CsI was deposited. Both types of ACS had a thin protective coating, which faced the optical sensor during x-ray exposure. The $a\text{-C}$ substrate side faced the x-ray source. Table I is a summary of the structures of the different CsI samples.

B. PHS measurements

PHS measurements were made on all four CsI samples. The experimental apparatus and methods were the same as that described in Ref. 19. Each CsI sample was placed directly at the input of the PMT (model R6095, Hamamatsu

TABLE I. Summary of structural difference between the four different CsI samples used in the PHS measurement. Backing refers to the optical interface of the CsI at the x-ray entrance side. Front refers to the side of the CsI that is in contact with the optical sensor, i.e., the PMT.

Sample	Substrate material	Backing	Front (Sensor contact)
FOS/HR	FOP		FOP
FOS/HL	FOP	Reflective	FOP
ACS/HR	$a\text{-C}$	Absorbing	Transparent coating
ACS/HL	$a\text{-C}$	Reflective	Transparent coating

Photonics Corporation), which detects and amplifies the light generated in CsI by each x-ray photon. The electronic signal at the output of the PMT was connected to a charge amplifier followed by a pulse-shaping amplifier. The final shaped pulse had an amplitude proportional to the charge output of the PMT. The final output signal was fed to a multichannel analyzer so that a PHS could be obtained. Monoenergetic x rays were used, which were generated by K fluorescence from selected elements.

C. Escape efficiency versus depth

Here we describe the method for extracting light escape efficiency (e) as a function of depth z from experimental measurements of PHS. With monoenergetic x rays with energy E less than the K -edge E_K , the variations in pulse heights observed in the PHS should be due only to the variations in e under the assumptions of: (1) the number of photons m originally created after absorption of an x ray of energy E is large enough that the noise in the photon creation process can be neglected; and (2) the broadening of the PHS due to noise in the detection by the PMT of the escaping and collected photons is small compared to broadening from the variation in the escape process itself.

Assumption (1) was originally made by Swank,⁷ and for a screen in prompt emission mode and at x-ray energies such that the photoelectron range is small compared to the thickness,⁷ should be reasonable. Assumption (2) can be tested by calculation, as in Drangova and Rowlands,¹⁷ which we outline here. As shown in Fig. 1, the number of electrons produced at the photocathode of the PMT for a particular pulse is

$$n_e = me\beta\eta_p, \quad (5)$$

where e is the escape efficiency, β is the optical coupling efficiency for collection of emitted photons between the CsI and the PMT, and η_p is the quantum efficiency of the PMT photocathode. At $E=30$ keV, taking the inherent energy required per photon for CsI(Tl) as ~ 20 eV (Ref. 19) results in m of ~ 1500 . Assuming a mean escape efficiency of 60%, and a light collection efficiency β between the CsI and the PMT of 80% results in a number of collected photons n_c of 720. With a photocathode quantum efficiency η_p of 10% (Ref. 19) for photons emitted from CsI(Tl), the number of electrons produced would be $n_e=72$. As will be shown in Sec. IV, the mean number of electrons per absorbed x ray finally detected by the PMT is $n_e \sim 70$ for the ACS HL sample. The normalized standard deviation in the number of electrons generated in the photocathode, due to statistical effects in detection, is then roughly estimated as $1/\sqrt{70} = 12\%$. This is small compared to the spread observed in the measured PHS for each CsI sample, which is estimated to be approximately $\pm 50\%$. Although the effect of PMT noise is not completely negligible, our original assumptions are reasonable. Later we will describe a method for removing the effect of PMT noise on the PHS measurements, so that the corrected PHS can be used to provide more accurate estimate of the Swank factor and e .

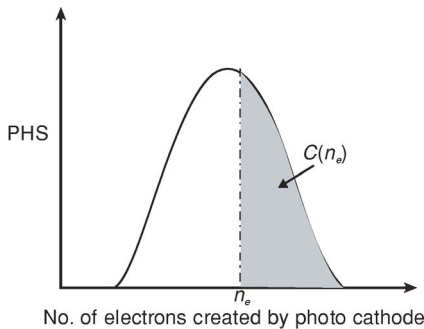


FIG. 4. Diagram illustrating the integration of the PHS to form the cumulative spectrum $C(n_e)$ for the derivation of escape efficiency vs depth.

Given the assumptions above, the observed width of PHS is due to variations in e versus depth z . If a monotonic change in e vs z is assumed, each value of n_e on the horizontal axis of the PHS corresponds to a unique value of depth z . We used the following method to determine $z(n_e)$, i.e., z as a function of n_e . As shown in Fig. 4, we denote the integration of the PHS for $n \geq n_e$ as $C(n_e)$, which corresponds to the number of x rays absorbed between the depths of $0-z$ from the origin at the exit surface. For the simplest case of x rays absorbed uniformly across the thickness L , the number of absorbed x-rays $C(n_e)$ is proportional to the layer thickness $z(n_e)$, and we obtain

$$z(n_e) = \frac{C(n_e)L}{N_q}, \quad (6)$$

where N_q is the total number of x rays absorbed in the entire phosphor layer given by

$$N_q = N_0(1 - e^{-\mu L}), \quad (7)$$

where N_0 is the number of incident x-ray photons and μ is the energy dependent linear attenuation coefficient for the phosphor. Once the depth z is determined for a given n_e value, the relative light escape efficiency for this depth can be calculated using $e = n_e/n_{e(\max)}$, where $n_{e(\max)}$ is the maximum number of detected electrons at a given x-ray energy. Note that the scale on the $e-z$ curves is not absolute, but relative to the maximum signal obtained, from the side of the screen nearest the detector.

We illustrate the above method schematically in Fig. 5, for clarity. Suppose that the x-ray absorption is uniform, and that the total number of absorption events were N . Each absorption event produces a large number of photons which

travel along various paths as illustrated, but whose average probability of reaching the front surface and escaping is constant for a given depth, and which we define as $e(z)$. Consider first the highest bin in the measured PHS, at $n_e=50$ electrons and suppose it has $N/10$ counts. Then this bin corresponds to x rays that were absorbed within the depths z from 0 to $L/10$, from the front surface. Taking $n_{e(\max)}$ as the number of electrons detected for this highest bin, we plot $e=1$, at z of $L/20 \pm L/20$. Consider next the second highest bin in the measured PHS, at $n_e=40$ electrons and suppose it has $3N/10$ counts. Then this bin corresponds to x rays that were absorbed between the depths of $L/10$ and $4L/10$ from the front surface. We plot $e=0.8$, at z of $5L/20 \pm 3L/20$, and similarly for the rest of the bins of the PHS histogram.

We can extend the above analysis to nonuniform (exponential) x-ray absorption. For the *front* screen geometry shown in Fig. 1, (so called because the photons are emitted from the side opposite to where the x rays enter), the $C(n_e)$ is given by

$$C(n_e) = N_0 [e^{-\mu(L-z)} - e^{-\mu L}]. \quad (8)$$

Substituting Eq. (7) into Eq. (8) we obtain

$$C(n_e) = \frac{N_q e^{-\mu L} (e^{\mu z} - 1)}{(1 - e^{-\mu L})}. \quad (9)$$

The value of N_q can be determined by integrating the entire PHS, which gives the total number of x rays detected in the experiment. Solving Eq. (9) for z , we obtain

$$z(n_e) = \frac{1}{\mu} \ln \left[1 + \frac{C(n_e)(e^{\mu L} - 1)}{N_q} \right]. \quad (10)$$

The following steps are used to derive e as a function of z from the measured PHS: (1) determine μ for the x-ray energy used in the PHS measurement; (2) calculate N_q by integrating the entire PHS to obtain the total number of x rays absorbed; (3) choose a value for n_e on the horizontal axis of PHS, and calculate $C(n_e)$ by integrating the PHS for $n \geq n_e$; and (4) calculate depth z for the given n_e , using Eq. (10) and determine e for this depth using $e = n_e/n_{e(\max)}$.

The above analysis assumed that the effect of PMT detector noise on the PHS measurements was negligible. Now we describe a method for estimating and removing the effect of PMT detector noise from the measured PHS, so that the $e-z$ curves can be extracted more accurately. As shown in Fig. 1, the mean number of photons collected by the PMT is n_c . Assuming that the input photon stream is noiseless, the

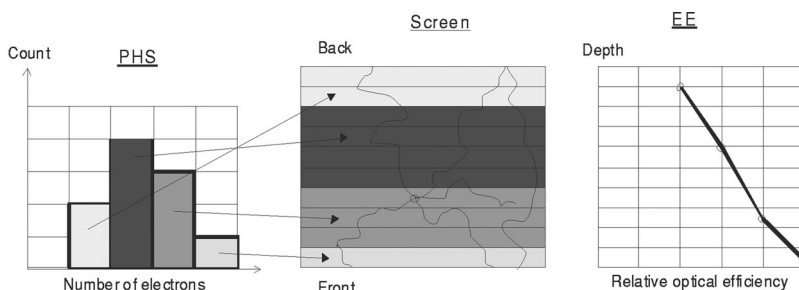


FIG. 5. Schematic illustrating the construction of the relative optical efficiency via the measured PHS.

number of photoelectrons created in the PMT, n_e , will vary due to the binomial distribution in the quantum absorption process of the photocathode, with efficiency η_p . The variance in the number of photoelectrons σ_{ne}^2 is then given by²⁰

$$\sigma_{ne}^2 = \eta_p(1 - \eta_p)n_c. \quad (11)$$

Further noise is added due to the statistical fluctuation in the gain of the PMT dynode chain, which is usually quantified as a multiplicative excess noise factor (NF) which multiplies the total variance given above. NF is dominated by the first dynode stage of the PMT, and can be estimated, for Poisson dynode statistics, from the first dynode gain δ using²⁰

$$NF \cong \delta/(\delta - 1). \quad (12)$$

For the PMT and power supply voltage used in our experiments, δ was estimated to be 3.76, resulting in a NF value of ~ 1.36 .²¹ The measured PHS, and the estimated PMT noise were both fitted to Gaussian functions. A corrected PHS was derived by deconvolution of the PMT noise. The $e(z)$ extraction procedure, as described above, was then repeated using the corrected PHS.

D. Calculating I_{OPD} from escape efficiency

The most straightforward method for obtaining the optical factor I_{OPD} is from the moments of the measured PHS using Eq. (3) for $E < E_K$, where I_{AED} can be assumed to be unity. Also, for energies $E > E_K$, the factor I_{AED} can be calculated by simulation of characteristic x-ray emission and reabsorption processes,²² and I_{OPD} can then be estimated indirectly using Eq. (4). However in screen optimization procedure, we sometimes only have the estimated light escape efficiency versus depth based on a particular screen design model. We will show here that I_{OPD} can also be obtained from the $e(z)$ curve. This will provide a theoretical means to determine the Swank factor for different screen designs without the need for explicitly calculating the PHS.

The amplitude of the scintillation pulse, i.e., the number of escaping light photons for each absorbed x ray, $n(z)$ is given by:

$$n(z) = m(E)e(z), \quad (13)$$

where $m(E)$ is the number of luminescent photons produced by absorption of an x ray of energy E in the material, and $e(z)$ is the escape efficiency from depth z . The j th moment of the optical scintillation spectrum is then

$$M_j = \int N_x(z)m^j e(z)^j dz, \quad (14)$$

where $N_x(z)$ is the number of x rays absorbed at depth z . Neglecting the nonuniformity in $N_x(z)$, we obtain

$$M_0 = N_x \int dz, \quad (15)$$

$$M_1 = N_x m \int e(z) dz, \quad (16)$$

and

$$M_2 = N_x m^2 \int e(z)^2 dz. \quad (17)$$

Then the optical factor becomes

$$I_{OPD} = \frac{M_1^2}{M_2 M_0} = \frac{1/L^2 \int e(z) dz^2}{1/L \int e(z)^2 dz}. \quad (18)$$

Equation (18) indicates that I_{OPD} (in the case of uniform x-ray absorption as a function of depth z) is determined by the square of the depth-average escape efficiency divided by the average square escape efficiency

$$I_{OPD} = \langle e \rangle^2 / \langle e^2 \rangle. \quad (19)$$

To demonstrate the derivation of I_{OPD} from $e(z)$, we used several simple examples of screen optics design: (1) *White backing turbid screen*: 100% reflectance for the screen backing, no bulk absorption and no internal reflection at exit; (2) *Black backing turbid screen*: 100% absorption for the screen backing, no bulk absorption and no internal reflection at exit; (3) *Linear escape efficiency*: $e(z)$ decreasing linearly with depth, with a mean value of \bar{e} and total variation $2\Delta e$, where $e(z)$ is given by

$$e(z) = \bar{e} - \Delta e \left(\frac{2z}{L} - 1 \right) \quad (20)$$

and (4), *Turbid screen with dye absorption added*: the case of added bulk absorption illustrated in Fig. 2(a).

IV. RESULTS AND DISCUSSION

A. PHS measurements

PHS measurements were performed for a range of incident x-ray energies between 25 and 50 keV. Shown in Fig. 6 are representative PHS measurements for the ACS HL sample at x-ray energies of 25, 30, 40, 43, 46, and 49 keV. Figure 6 shows that at $E > E_K$ of Cs and I (36 and 33 keV, respectively), there is a second peak in the PHS due to the escape of K -fluorescence photons. Since the purpose of this article is to investigate I_{OPD} and extract the light escape efficiency for different screen designs, only the PHS for $E < E_K$ were used. The effect of K fluorescence is avoided which simplifies the data analysis. The measured PHS for all four CsI samples are shown in Fig. 7 for $E=25$ and 31 keV. The PHS are plotted as the number of counts $P(n_e)$ versus the size of the scintillation pulse n_e (given in number of electrons detected by the PMT). The FOS samples were coupled to the PMT through the FOP substrate, which had an optical transmittance of 60%. The ACS samples were coupled to the PMT through a transparent protective coating, which had minimal attenuation of light. To allow for easier comparison between the FOS and ACS sample types, the PHS for the FOS samples (HL and HR) are replotted in Fig. 8 after correction for the 60% FOP transmittance. Figure 8

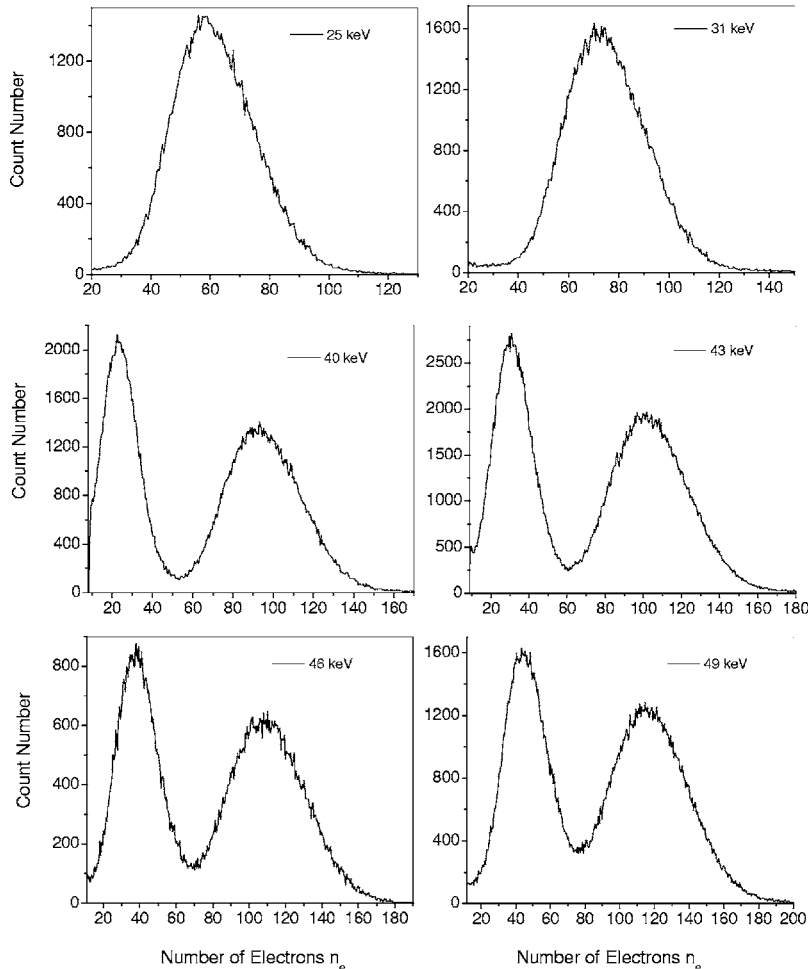


FIG. 6. Measured PHS for the ACS HL sample at six different x-ray energies.

shows that, after correction, the ACS HL sample produced the most light photons per x ray, and FOS HR and ACS HR the least. Although the mean light output from the ACS HR is comparable to that from the FOS HR, it has a broader distribution in the PHS. Given that the PHS measurements for all four samples were made using the same apparatus, and the samples were made with the same scintillating material, it can be concluded even before detailed analysis that the magnitude of e was markedly different between screen types.

B. Escape efficiency versus depth

1. Without PMT noise correction

The PHS measurements of the four CsI samples were used to obtain e - z curves. The results are shown in Fig. 9, for $E=25$ and 31 keV. Figure 9 shows that the e - z curves derived from the two sets of PHS measurements at $E=25$ and 31 keV are nearly identical, supporting the theory⁸ that the optical escape process is independent of the incident x-ray energy. The value of e decreases approximately linearly with z for all the CsI samples. There is some bending in the curves at the high and low ends of z , which correspond to the tails of the PHS. In an ideal system with no photon noise and no measurement noise, an $e(z)$ which was perfectly linear with depth would result in a PHS with a flat top, and vertical

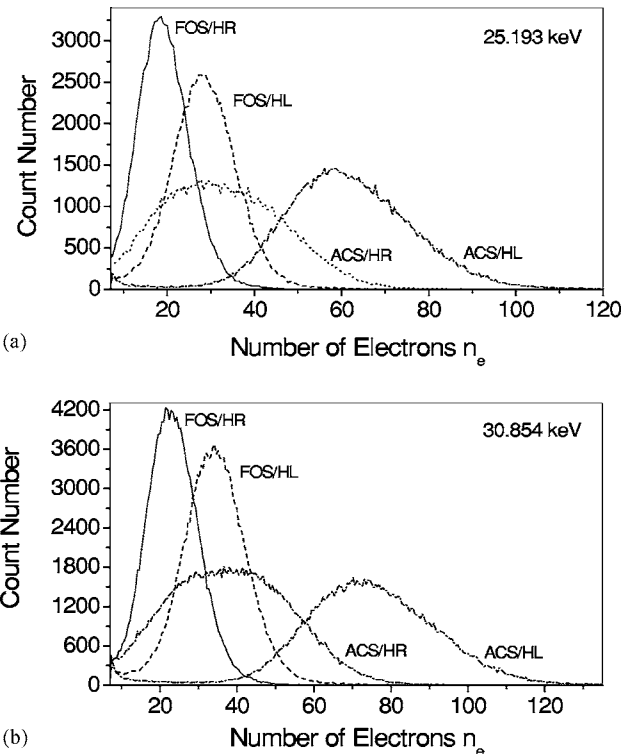


FIG. 7. (a) Measured PHS for four different CsI samples at $E=25$ keV. (b) Measured PHS for four different CsI samples at $E=31$ keV.

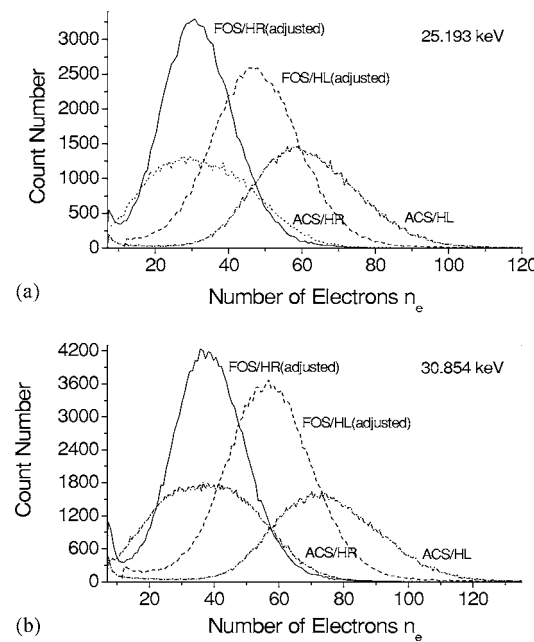


FIG. 8. (a) Measured PHS for four different CsI samples, with results for the FOS samples adjusted to account for optical transmittance of FOP substrate at $E=25$ keV. (b) Measured PHS for four different CsI samples, with results for the FOS samples adjusted to account for optical transmittance of FOP substrate at $E=31$ keV.

edges. In reality noise sources exist, resulting in unsharpness in the PHS edges and bending in the derived e - z curves. In the next section the effect of measurement noise on the observed PHS and derived e - z curves is addressed.

It should also be understood that the *relative optical efficiency* plotted in Fig. 9 is not an *absolute* number, but a fraction relative to the highest experimentally observed number of detected electrons, $n_e(\max)$. There is some uncertainty (10%) in picking $n_e(\max)$ because of the unsharpness in the edges of the measured PHS.

2. With PMT noise correction

It should be noted that the uncorrected PHS measurements shown in Fig. 7 were used to estimate the effect of PMT detector noise. Figure 10 shows the comparison between the measured PHS of the ACS HL sample and its Gaussian fitting, which is in reasonable agreement with the measurement and facilitates the deconvolution process for removing the effect of PMT noise from the PHS measurements. Also shown in Fig. 10 is the PMT noise corrected PHS, which is narrower than the original PHS measurement data. The $e(z)$ derived from the corrected PHS are shown in Fig. 9(c) for $E=25$ keV. It can be seen that the bending in the curves at the high and low ends of z , as well as the slope of the curves in the linear region, are both reduced compared to the uncorrected results in Fig. 9(a).

Screen optics models provide a link between $e(z)$ and optical design parameters, e.g., substrate reflectance or bulk absorption. Such models⁸ have been useful for the optimization of systems employing powdered phosphor screens.¹³ Rowlands and Yorkston² have shown in arguments supported

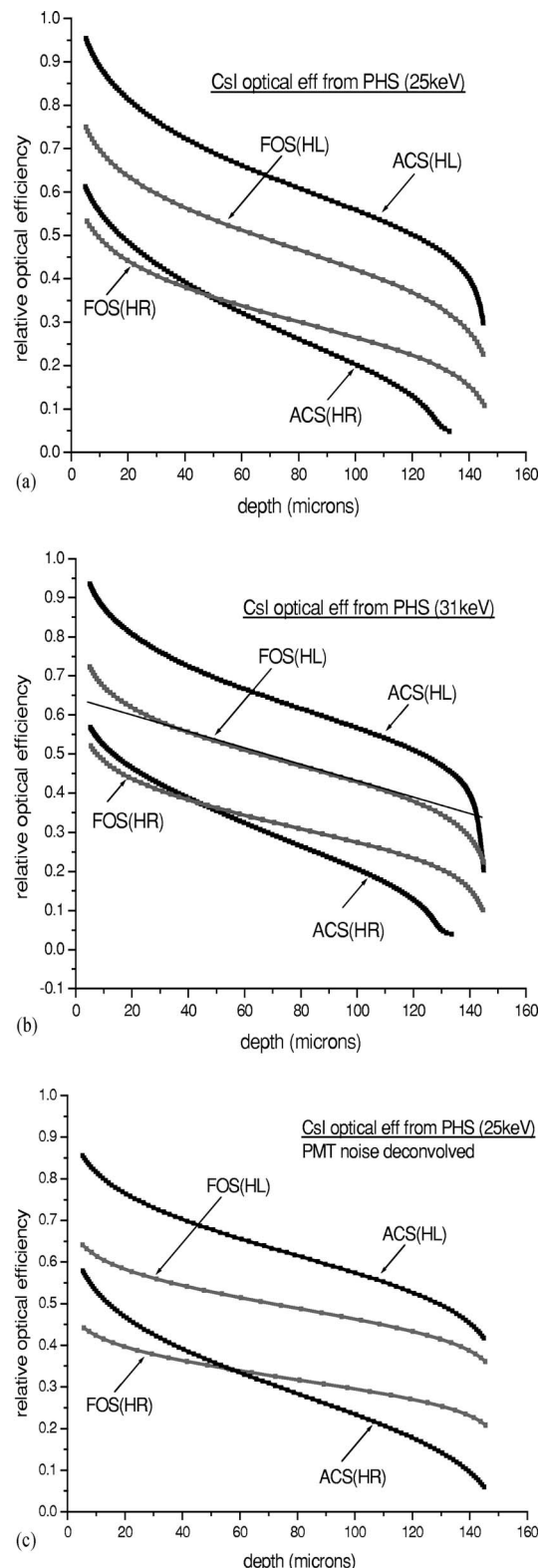


FIG. 9. Light escape efficiency vs depth derived from the measured PHS for four CsI samples at: (a) $E=25$ keV; (b) $E=31$ keV; and (c) $E=25$ keV, with PHS corrected for the effect of PMT noise.

by experimental data that, although CsI screens exhibit better spatial resolution than powder screens of the same thickness, they show an optical behavior intermediate between a perfect

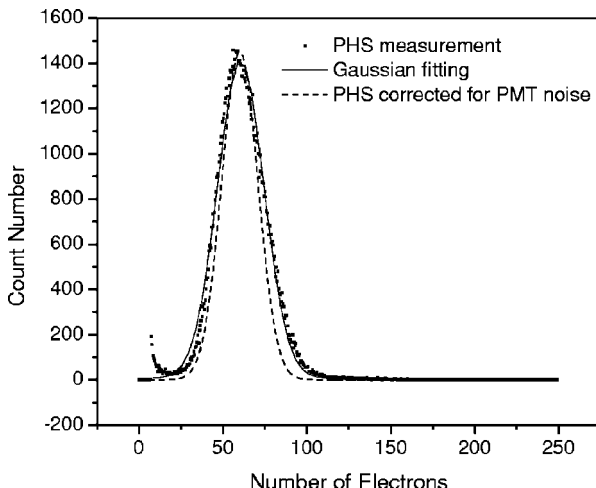


FIG. 10. Comparison of PHS with and without PMT noise deconvolution. The data points are the measured PHS for the ACS HL sample. The solid line is a Gaussian fit to the PHS data, and the dashed line (with smaller width) is the PHS corrected for PMT noise.

fiber optic and a turbid screen, with MTF decreasing with increasing thickness. Although it would be helpful to develop analytic physical models for anisotropic (columnar structured) screens like CsI, we may, with caution, use insights from the isotropic powder models to help interpret the derived $e(z)$ curves. For example, the $e(z)$ for ACS HR in Fig. 9 above drops to near zero at the backing, whereas ACS HL has a generally higher $e(z)$ in the bulk, approaching a non-zero value, for z near the back. These are the kinds of behavior expected (as in Fig. 2) for screens comprising phosphors on nonreflecting and reflecting substrates, respectively. The model interpretation is in agreement with the optical design of the ACS HR and ACS HL samples, which are optimized for high resolution and high light output, respectively. If we compare the two screens optimized for high resolution we find that compared to the ACS HR, and also in contrast to the predicted $e(z)$ behavior for a turbid phosphor HR screen with a nonreflective backing, the FOS HR has an $e(z)$ that varies much less versus z . The substantially lower $e(z)$ of the ACS HR near the back is because the CsI layer was deposited on a black substrate (*a-C*), which has much higher optical absorption. The reduced z dependence of $e(z)$ for the structured phosphor FOS HR screen, compared to the strong depth dependence expected for powder screens with nonreflective backings shown in Fig. 2(b), is in agreement with predictions based on Monte Carlo calculations for light scattering in homogeneous compared to columnar screen structures.²³ This behavior is due to partial waveguiding of light up and down the columns.

C. Calculating I_{OPD} from escape efficiency

The $e(z)$ curves for the first three simple cases listed in Sec. III D: (1) 100% reflectance for the screen backing, no bulk absorption, no internal reflection at exit; (2) 100% absorption for the screen backing, no bulk absorption, no internal reflection at exit; and (3) $e(z)$ decreasing linearly with z ,

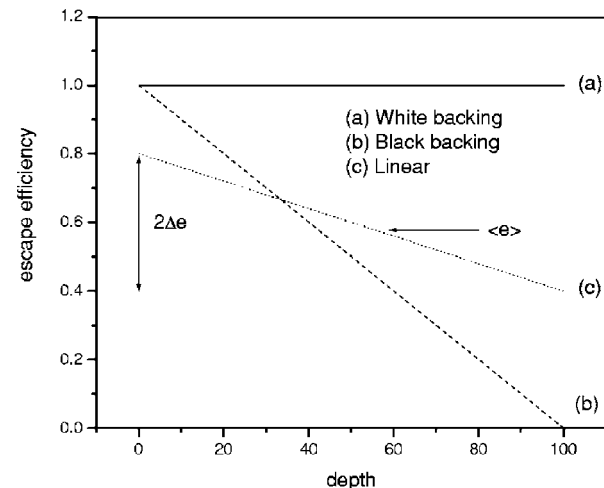


FIG. 11. Schematic illustration of the escape efficiency vs depth for three simple cases: (a) 100% backing reflectance, no bulk absorption or internal reflection at exit; (b) 100% backing absorption, no bulk absorption or internal reflection at exit; and (c) escape efficiency decreases linearly vs depth.

are shown in Fig. 11. The $e(z)$ for the first case is unity across the full range of z , resulting in $I_{OPD}=1$. The $e(z)$ for the second case decreases from unity at $z=0$ to zero at the back of the screen, i.e., $z=L$, and we obtain $I_{OPD}=0.75$, as originally pointed out by Swank.⁸ For the third case, I_{OPD} can be derived using Eqs. (19) and (20) as

$$1/I_{OPD} = 1 + (1/3)(\Delta e/\bar{e})^2. \quad (21)$$

For the fourth simple case of added bulk absorption illustrated in Fig. 2(a), the calculated I_{OPD} decreases from 0.75 to 0.30 with increasing bulk absorption for the examples shown. By adding even more bulk absorption, the Swank factor can eventually be reduced to zero in the limit of high optical absorption.

For the linear case, as shown in Eq. (21) above, I_{OPD} depends only on the fractional variation in $e(z)$. Thus in this case, either improving \bar{e} at a constant Δe , or reducing Δe at a constant \bar{e} , will both improve I_{OPD} . The experimental CsI screens above have derived $e(z)$ curves that resemble the linear case. For the results in Fig. 9, the $e(z)$ curves were fitted with a straight line, as shown for example in Fig. 9(b), and the I_{OPD} from Eq. (21) was compared with that obtained in the usual way from the moments of the PHS. The results were generally equivalent, as shown in Table II.

The I_{OPD} was also calculated for each sample, using the PHS that were corrected for the PMT detector noise (as described in Secs. III C and IV B). The results are shown in Table II. Neglecting the detector noise underestimates I_{OPD} by 5%–10% for the FOS samples, and by <3% for the ACS samples, which had a wider PHS distribution than the FOS samples. From the $e(z)$ curves in Fig. 9(c), it can be seen that the FOS HR and FOS HL have essentially the same Δe , and the higher \bar{e} for the FOS HL sample leads to a slightly higher I_{OPD} . Although the ACS HL has a slightly larger Δe compared to the FOS samples, it has an I_{OPD} value comparable to that of the FOS samples because it has the highest \bar{e} for all

TABLE II. Comparison of optical excess noise factors obtained from measured Pulse Height Spectra for CsI:T1 samples of various optical designs, with the noise factors obtained from (i) measured uncorrected Pulse Height Spectra, (ii) linear fit to uncorrected derived e - z curves, (iii) Pulse Height Spectra corrected for the effect of PMT detector noise.

Sample	From uncorrected PHS	From linear fit to (uncorrected) e - z curve	From corrected PHS
FOS/HR	0.90	0.91	0.97
FOS/HL	0.93	0.94	0.98
ACS/HR	0.86	0.82	0.86
ACS/HL	0.94	0.95	0.97

the samples used in our experiments. The ACS HR sample, which has the highest Δe due to its absorptive backing, has the lowest I_{OPD} .

The goal of our investigation is to understand the interplay of screen parameters so as to permit the optimization of the performance of CsI layers for different DR detector applications. It can be seen from Eq. (2) that to optimize the DQE(0), we need to maximize both the quantum absorption efficiency η and the Swank factor A_S . Equation (20) shows that to maximize I_{OPD} , we need to maximize the mean escape efficiency \bar{e} , and minimize its variation Δe . Screen optics models indicate that one way to accomplish this is to use a screen with high quantum gain m , minimal bulk absorption and a highly reflective backing. For the four samples used in our experiment, the two ACS samples have larger Δe , corresponding to a larger variation of e with depth. The ACS HL, FOS HL, and FOS HR samples all provide very high levels of I_{OPD} and A_S .

It is noted that the I_{OPD} values obtained for the CsI samples are quite high, i.e., ≥ 0.9 except for ACS HR. These values compare favorably with the range of I_{OPD} of 0.6–0.9 for good quality powder phosphor screens.¹⁸ The higher I_{OPD} for CsI is most likely connected with the light channeling properties of the CsI needle structure, which evidently reduces the variation of escape efficiency with depth. This may be due to reduced optical path length and bulk absorption for photons produced at some depth from the exit surface because their travel is at least partially restricted to columnar paths.

To optimize the performance of an imaging detector, in which performance at finite spatial frequencies is important, we must go further than DQE(0) and consider the DQE as a function of spatial frequency. This will be the subject of future work.

V. CONCLUSIONS

A theoretical model was developed for the light escape efficiency of x-ray scintillators, and a method for deriving $e(z)$ from PHS was described. The method was applied to experimental PHS measurements from CsI samples with four different designs. The results showed that $e(z)$ varies essentially linearly as a function of z in the CsI samples, and that the magnitude of variation is relatively small, leading to very high values for both the I_{OPD} and Swank factor. The effect of

PMT noise on PHS measurement was estimated and found to result in a small but noticeable underestimation ($\sim 5\%$) of the Swank factor.

ACKNOWLEDGMENTS

The authors gratefully acknowledge financial support from the NIH (5 R01 EB002655-02) and the U.S. Army Breast Cancer Research Program (W81XWH-04-1-0554). They are grateful to G. DeCrescenzo for helpful discussions and advice.

^aElectronic mail: arl@mil.sunysb.edu

¹L. E. Antonuk, Y. El-Mohri, J. H. Siewerdsen, J. Yorkston, W. Huang, V. E. Scarpine, and R. A. Street, "Empirical investigation of the signal performance of a high-resolution, indirect detection, active matrix flat-panel imager (AMFPI) for fluoroscopic and radiographic operation," *Med. Phys.* **24**, 51–70 (1997).

²J. A. Rowlands and J. Yorkston, "Flat panel detectors for digital radiography," in *Medical Imaging*, Volume 1. Physics and Psychophysics, edited by J. Beutel, H. L. Kundel, and R. Van Metter (SPIE, Bellingham, WA, 2000), pp. 223–328.

³W. Zhao and J. A. Rowlands, "Digital radiology using active matrix read-out of amorphous selenium: Theoretical analysis of detective quantum efficiency," *Med. Phys.* **24**, 1819–1832 (1997).

⁴J. H. Siewerdsen, L. E. Antonuk, Y. El-Mohri, J. Yorkston, W. Huang, and I. A. Cunningham, "Signal, noise power spectrum, and detective quantum efficiency of indirect-detection flat-panel imagers for diagnostic radiology," *Med. Phys.* **25**, 614–628 (1998).

⁵D. P. Traurnicht and J. Yorkston, "Screen design for flat-panel imagers in diagnostic radiology," *Proc. SPIE* **3336**, 477–484 (1998).

⁶J. A. Rowlands, W. G. Ji, and W. Zhao, "Effect of depth dependent modulation transfer function and K-fluorescence reabsorption on the detective quantum efficiency of indirect conversion flat panel x-ray imaging systems using CsI," *Proc. SPIE* **4340**, 257–267 (2001).

⁷R. K. Swank, "Absorption and noise in x-ray phosphors," *J. Appl. Phys.* **44**, 4199–4203 (1973).

⁸R. K. Swank, "Calculation of modulation transfer functions of x-ray fluorescent screens," *Appl. Opt.* **12**, 1865–1870 (1973).

⁹R. E. Marshak, H. Brooks, and H. Hurwitz, Jr., "Introduction to the theory of diffusion and slowing down of neutrons," *Nucleonics* **4**, 10–22 (1949).

¹⁰H. C. Hamaker, "Radiation and heat conduction in light scattering materials," *Philips Res. Rep.* **2**, 55–67 (1947).

¹¹P. Kubelka and F. Munk, "Ein Beitrag zur Optik der farbanstriche," *Z. Tech. Phys. (Leipzig)* **12**, 593–601 (1931).

¹²A. Schuster, "Radiation through a foggy atmosphere," *Astrophys. J.* **21**, 1–22 (1905).

¹³A. R. Lubinsky, J. F. Owen, and D. M. Korn, "Storage phosphor system for computed radiography: Screen optics," *Proc. SPIE* **626**, 120–132 (1988).

¹⁴L. Yang and S. J. Miklavcic, "Revised Kubelka-Munk theory. III. A General theory of light propagation in scattering and absorptive media," *J. Opt. Soc. Am. A Opt. Image Sci. Vis.* **22**, 1866–1873 (2005).

¹⁵B. K. C. Lum, M. Sc. Thesis, University of Arizona, 1980.

- ¹⁶C. E. Dick and J. W. Motz, "Image information transfer properties of x-ray fluorescent screens," *Med. Phys.* **8**, 337–346 (1981).
- ¹⁷M. Drangova and J. A. Rowlands, "Optical factors affecting the detective quantum efficiency of radiographic screens," *Med. Phys.* **13**, 150–157 (1986).
- ¹⁸D. P. Traurnicht and R. Van Metter, "The measurement of conversion noise in x-ray intensifying screens," *Proc. SPIE* **914**, 100–116 (1988).
- ¹⁹Wei Zhao, G. Ristic, and J. A. Rowlands, "Inherent imaging performance of cesium iodide scintillators," *Med. Phys.* **31**, 2594–2605 (2004).
- ²⁰R. W. Engstrom, *RCA Photomultiplier Handbook* (RCA Corporation, Lancaster, 1980).
- ²¹C. Watt, K. Yan, G. DeCrescenzo, and J. A. Rowlands, "The physics of computed radiography: Measurements of pulse height spectra of photo-stimulable phosphor screens using direct luminescence," *Med. Phys.* **32**, 3589–3598 (2005).
- ²²W. Zhao, W. G. Ji, and J. A. Rowlands, "Effects of characteristic x-rays on the noise power spectra and detective quantum efficiency of photoconductive x-ray detectors," *Med. Phys.* **28**, 2039–2049 (2001).
- ²³A. Badano and R. Leimbach, "Depth-dependent phosphor blur in indirect x-ray imaging sensors," *Proc. SPIE* **4682**, 94–106 (2002).